

Copyright

by

Sean Matthew Lewis

2013

**The Thesis Committee for Sean Matthew Lewis
Certifies that this is the approved version of the following thesis:**

**Megagauss 2.0: a System for Production of Megaamp Currents and
Megagauss Fields for Laser Plasma Experiments**

APPROVED BY
SUPERVISING COMMITTEE:

Roger Bengtson, Supervisor

Todd Ditmire

**Megagauss 2.0: a 10 Capacitor System for Production of
Megagauss Fields for Laser Plasma Experiments**

**By
Sean Matthew Lewis, B. S.**

Thesis

Presented to the Faculty of the Graduate School

The University of Texas at Austin

In Partial Fulfillment

of the Requirements

for the Degree of

Master of Arts

THE UNIVERSITY OF TEXAS AT AUSTIN
May 2013

Acknowledgements

First, to my family, the foundation and mental basis of all that I do. They raised me to feed my curiosity, and subsequently backed my obscure pursuit thereof, even when it meant my absence.

To the people in the Ditmire group who have spent so much of their lives on these tricky and troublesome devices, the lasers. To Sam Feldman and Matt McCormick, for their help on GHOST. To Dr. Hernan Quevedo, for always being there when I had a question, and always having a useful and informative answer. To Dr. Ditmire, my unofficial adviser, a laser man for the record books if ever there was one.

To the folks at Sandia National Laboratories who mentored me and taught me so much about the technology I would need to use. To Dr. Kenneth Struve, for kindling my interest in the potential of pulsed power. To Brian Stoltzfus, for tolerating my ignorance of pulsed power and helping to alleviate it.

To Matthew Wisher, my friend and colleague, who is co-responsible for a large portion of the original work presented here.

Finally to Dr. Roger Bengtson. A kinder adviser and more supportive man I could not imagine. Roger was there every step of the way with knowledge and patience to spare. Roger was there when I most needed support; when things became trying and I was ready to give up.

To all these great people I owe acknowledgement, and the hope that my small work here are worthy of their approval.

Abstract

Megagauss 2.0: a System for Production of Megaamp Currents and Megagauss Fields for Laser Plasma Experiments

Sean Matthew Lewis, M.A.
The University of Texas at Austin, 2013

Supervisor: Roger Bengtson

High magnetic fields greater than 100 Tesla applied to laser generated plasmas can generate unique and interesting conditions. High power laser systems at the University of Texas in the Center for Higher Energy Density Sciences readily produce short lived fusion plasmas in cluster targets. A strong magnetic field could increase fusion neutron yield and plasma confinement while providing a unique plasma physics environment.

For this purpose, Sandia National Laboratories in collaboration with the University of Texas designed and constructed a pulsed power device to produce more than 2 megaamperes. This current produces strong magnetic fields in small coils with duration on the order of microseconds. At the University of Texas, tests with this device determined the operational characteristics. I will describe the behavior of this device with currents of approximately a megaamp and magnetic fields of more than 60 Tesla. Emphasis is placed on understanding the behavior of the fields and coils.

Contents

Acknowledgements

Abstract

List of Figures

Chapter 1: Introduction	1
1.1 Introduction	1
1.2 Scientific motivation	2
Chapter 2: Physics Background	3
2.1 Cluster fusion and coulomb explosions	3
2.2 Cluster fusion in a magnetic field.....	6
2.3 Magnetic field requirements	10
2.4 Context for megagauss field drivers: other facilities	11
Chapter 3: Basic Megagauss System Design	14
3.1 Experimental setup	14
3.2 Driver requirements restated	17
3.3 Upgrade to Full current 10-capacitor system.....	17
3.4 Basic RLC Circuit.....	18
3.5 Capacitance	19
3.6 Inductance	20
3.7 Resistance	22
3.8 Practical System capabilities.....	22
3.9 Low current mode of operation.....	22
Chapter 4: Full-Current System Hardware Specifics and Controls	24
4.1 Switch can assemblies	24
4.2 Switches.....	26
4.3 Trigger system	27
4.4 Charging and dump relay tank	29
4.5 Electronics control rack	31
4.6 Voltage sensing and b-dots	34
4.7 Vacuum chamber	36
4.8 Modifications to the chamber for full-current system	37

4.9 Safety measures	38
Chapter 5: Results from Megaamp Destructive Shots	41
5.1 Switch b-dot calibration	41
5.2 Full system shot tests	42
5.3 Megaamp shots with coils in atmosphere	43
5.4 Failure modes in atmosphere	44
5.5 System inductance comparison to models	46
5.6 Vacuum operation	46
5.7 Vacuum operation failure modes	47
5.8 Sensitivity of transmission line breakdown to chamber pressure	49
5.9 Reduced current nondestructive shots	49
Chapter 6: Coil Behavior	50
6.1 Coils	50
6.2 Coil clamp	51
6.3 Mechanism of coil explosion	52
6.4 Coil expansion velocity measurement	53
6.5 Qualitative description of coil behavior	54
6.6 Skin effect	56
6.7 Comparison to simulations and other experiments	56
6.8 Expected field from known currents	58
Chapter 7: Faraday Rotation Measurements	61
7.1 Physics background	61
7.2 Experimental setup	63
7.3 MATLAB analysis	66
7.4 Results in Atmosphere	68
7.5 Field as a function of position on the z-axis	71
Chapter 8: Conclusions	76
Appendix A: Pre-shot checklist	78
Appendix B: Post-shot checklist	80
Bibliography	81
Vita	85

List of Figures

2.1 Cluster fusion yield as a function laser energy	5
2.2 Magnetic fields necessary for beta equal to one	11
3.1 Schematic of overall experimental setup	14
3.2 Schematic of chronology and timescales	16
3.3 The completed full system at UT.....	18
4.1 Switch can assembly	26
4.2 Titan 40364 switch and trigger resistor	27
4.3 Trigger box	29
4.4 Relay tank	30
4.5 Control rack	33
4.6 Overall megagauss circuit diagram	35
4.7 Vacuum chamber cross section	37
4.8 Transmission line modification for 60 cables	38
4.9 Safety grounding pin	40
5.1 Stainless shorting bar after mega amp shot	42
5.2 Sum switch currents from first MA shot	43
5.3 Copper coil debris after a 1.1 MA shot	44
5.4 Atmosphere breakdown aftermath	45
5.5 Coil remnants from successful vacuum shot	47
5.6 Current trace from a failed vacuum shot	48
6.1 Typical coils	51
6.2 Fast Camera image of coil expansion	54
6.3 Slotted coil fragments from megaamp shot	55
6.4 Simulated coil comparison	57

6.5 A bowed coil	57
6.6 Field profiles	60
7.1 Coil and crystal setup	65
7.2 Experimental layout	66
7.3 Raw oscilloscope rotation data	69
7.4 Plots of field and current as a function of time	70
7.5 Measured field as a function of z-axis position	71
7.6 Field as a function of position and comparison with data	74
7.7 Current model on the z-axis.....	75
7.8 Averaged field profiles from current models.....	75

List of Tables

3.1 system inductances	21
3.2 circuit parameters	21

Chapter 1: Introduction

1.1 Introduction

Laser-cluster interactions leading to fusion have been studied since the late 1990s and represent a compact, economical and novel way of achieving thermonuclear neutrons [1, 2, 3]. Even these first papers suggested that a strong magnetic field might augment the fusion neutron yield if they can improve the confinement time [2]. In these experiments, a high intensity and high power chirped-pulse amplified laser is focused on a gas jet containing deuterium clusters with overall number density near atmospheric density. Through Coulomb explosion interactions produce hot ions with temperatures sufficient for fusion reactions [4]. This creates measurable neutrons through the DD fusion branch that produces a 2.45 MeV neutron and a triton [2].

The resulting plasma expands rapidly, and all fusion reactions are over in times on the order of hundreds of picoseconds, with the greatest neutron production peak occurring in less than 100 ps [3] [5]. However, a sufficiently strong magnetic field may confine this plasma and increase neutron yield by a factor of 2-5 or more, depending on geometry. This experiment will study neutron production and plasma physics in such a magnetic field. Novel regimes of plasma in multi-keV temperature, atmospheric density highly magnetized plasmas will be accessible. Unique to these experiments is the ability to create fusion temperature plasmas in picoseconds with a magnetic field already in place [6]. Diagnostics will examine neutron production and plasma transport in this high field environment.

This thesis will describe the hardware and early experimental results for the driver

apparatus capable of producing a magnetic field for cluster fusion studies. Additional background on the science in the experiment is in the first chapter. Chapters two and three will describe details of the magnetic field driver. Further chapters will elaborate on technical details, problems, and results thus far, including magnetic field measurements.

1.2 Scientific Motivation

The plasma physics questions available to explore with this experimental setup are diverse. The first full laser and pulsed power experiments will focus on diagnosing neutron yield with plastic scintillator detectors and measuring plasma transport with optical techniques.

Neutron yield gain from the magnetic field may be affected by magnetic field geometry. Simulations from between 2006 and 2009 by Moustazis, Lalousis, and Loupasakis at the Technical University of Crete indicate that a magnetic field can significantly increase the plasma confinement to timescales approaching tens of nanoseconds. Their MHD code indicates that mirror trapping should be beneficial. Comparing plasma transport to these models should be possible [7] [8].

Several novelties also make this magnetized plasma unique. The large relative ion Larmor radius and electrostatic confinement of the ions may produce interesting physics [6]. Unusual effects of a large initial imbalance in density and space charge can be explored as the magnetic field affects their evolution [6]. There is also a possibility of producing small scale plasma jets or using these plasmas studying propulsion [7] [8]. So studying plasma axial transport may be fruitful. Finally, a high neutron flux per shot could be useful for neutron radiation damage materials studies. If sufficient neutron flux of more than 10^9 *n/shot* is present, the possibility opens to study radiation damage in future fast pump-probe experiments [9].

Chapter 2: Physics Background

2.1 Cluster Fusion and Coulomb Explosions

In cluster fusion experiments the hot fusion plasma is produced through Coulomb explosion of molecular clusters in a gas jet containing deuterium. The mechanism uses fast, intense laser pulses with intensity of 10^{17} W/cm^2 or more and pulse widths on the order of a hundred femtoseconds or less to irradiate solid density clusters in the gas jet [3]. Atoms are quickly ionized through tunneling ionization. Then electrons are expelled from the cluster at high velocity by the extremely intense laser field. The resulting electrostatic potential of the ions left behind causes them to explode at the multi-keV temperatures necessary for fusion [2] [3].

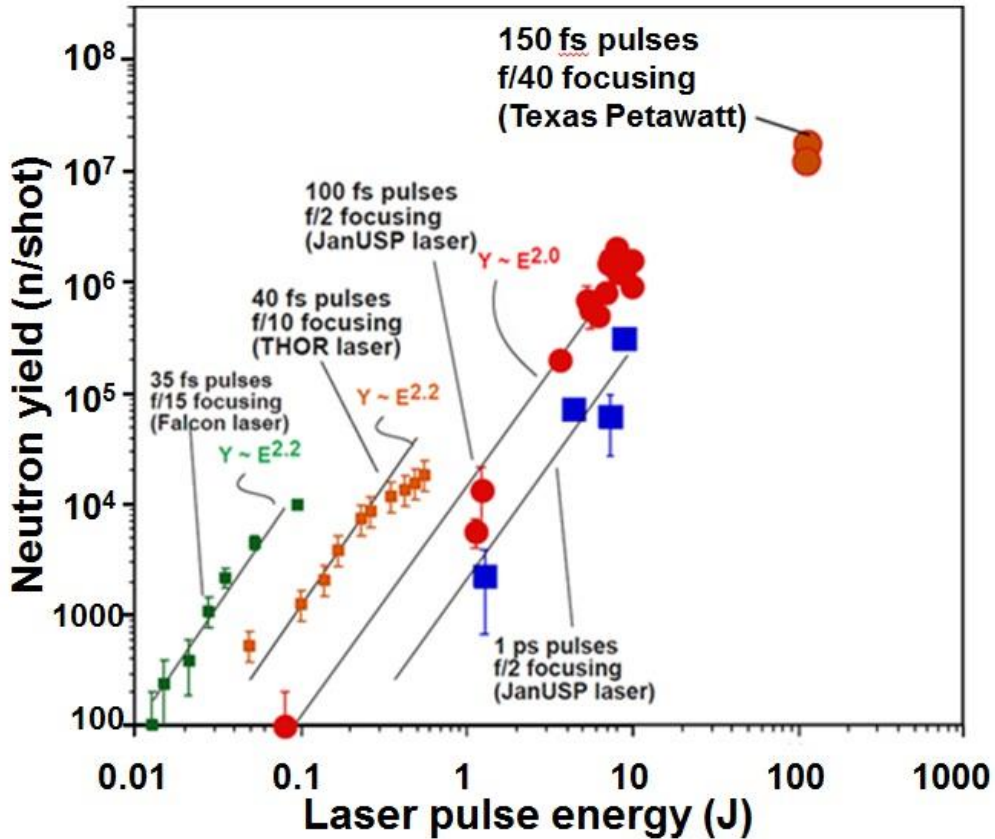


Figure 2.1 The benefit of increasing laser energy for cluster fusion neutron production is significant. As long as pulses are sufficiently short for the coulomb explosion mechanism, neutron yield seems to scale approximately like laser energy squared [10] [11].

The details of the Coulomb explosion can be explained simply. Cluster size is much smaller than the wavelength of the laser so the laser field is effectively uniform. This field draws out electrons in the cluster with each successive laser field oscillation. With a laser of sufficient intensity, electrons are unlikely to re-enter the cluster. If the laser pulse is sufficiently short in duration, all the cluster's electrons are removed within a few laser cycles. Although lower intensity regimes for laser-cluster interactions exist in which electrons are incompletely stripped or electrons oscillate inside the cluster and causing heating, this is not the regime of Coulomb explosions [12] [13].

As the laser ramps up on a timescale of tens of femtoseconds, more and more electrons

are expelled. First a shell of high potential exploding ions surrounds a neutral core which oscillates with the laser field. Then as all the electrons become stripped the neutral core disappears, causing total explosive disassembly of the cluster [12] [13] . A short-pulse laser is needed to remove electrons in timescales close to the cluster dis-assembly time, which is on the order of tens of femtoseconds. In general, ion energies depend on the ratio of the ionization time to the time of cluster expansion. This means laser pulses of high power are desirable [14].

Coulomb explosions allow efficient absorption of laser energy. The fraction of laser beam energy deposited into ion energy is usually more than 90% [3]. This property makes molecular cluster targets interesting for tabletop laser-plasma experiments. In addition, data from multiple laser systems seems to indicate that fusion neutron yield scales nearly as laser energy squared [10]. This scaling has motivated cluster fusion experiments already carried out on the Texas Petawatt Laser, which has energies of about 100-180 J and pulse duration of 120-170 fs [15]. Recent experiments by Bang indicate a neutron yield exceeding 10^7 neutrons per shot [16].

Releasing gas at high backing pressure through a pulse valve nozzle into vacuum creates the cluster targets. This gas expands and rapidly adiabatically cools. Van Der Waals forces cause the molecules to agglomerate to form clusters of thousands of atoms. The size of the clusters and number density of the gas varies depends on the gas jet nozzle and backing pressure [4] [17] [18]. The strength of Van Der Waals forces depends on atomic species while clustering depends on temperature. The average number of atoms per cluster follow the Hagen's empirical formula,

$$N = 33\left(\frac{\Gamma^*}{1000}\right)^{2.35}$$

where Γ^* is the Hagen parameter, which has been verified for cluster sizes of $\Gamma^* < 10^4$ [17] [18].

The gasses in these experiments are either cryogenic molecular deuterium (DD) or deuterated methane (CD^4). In order for deuterium to form clusters large enough to achieve the

necessary ion energies for fusion, it must be cryogenically cooled to temperatures approaching that of liquid nitrogen (77K) [2] [3]. CD^4 has stronger Van Der Waals bonding, and can cluster to the necessary size without cryogenic cooling [11]. CD^4 may be preferable to DD gas for this convenient reason.

The ion temperature is highly dependent on cluster size, with the largest clusters producing the hottest ions. 7.5 nm diameter clusters are at the threshold radius for producing 10 keV deuterium ions [6]. To ensure that clusters of sufficient size are created, the gas jet must have significant backing pressure; typically about 50atm or more than 700 psi [2] [3]. We suspect that obstructions in the path of the cluster, as will be required for magnetic field production, could hinder cluster formation [6] [19].

When ion temperatures from Coulomb explosions exceed a keV, fusion reactions can take place between ions colliding in the short-lived plasma after clusters have exploded. Reactions occurring in the hot plasma produce thermonuclear neutrons. Reactions involving hot ions with surrounding cold gas or cold plasma produce beam-target neutrons [11]. The relevant fusion reactions are:



Both reactions are equally likely, but neutrons are detectable only from the second reaction [2]. Details of cluster fusion depend heavily on the distribution of cluster sizes and their local density when the laser strikes [11] [16]. These details are beyond the scope of this thesis.

2.2 Cluster Fusion in a Magnetic Field

Cluster fusion yield is highly limited by confinement time. Without a magnetic field there is only inertial confinement; the plasma confinement time is just the time it takes the ions to

traverse the plasma at sound speed in all directions. In the radial direction for a long, narrow, cigar shaped plasma of radius 100 μm (determined by laser focal spot and energy) the ions traveling at sound speed would be expected to escape the original volume in 100 ps or less [6]. On early experiments with these narrow plasmas, high resolution neutron time of flight experiments indicate that the majority of fusion events are over in less than 100 ps, as expected from the traverse time estimates [5]. Texas Petawatt experiments have taken advantage of greater beam energy to perform fusion experiments away from best focus while still having intensities sufficient for cluster fusion. These plasma radii approach 1-2mm. These plasmas have higher neutron yields with a greater number of hot ions present. The ion traverse time is still on the order of hundreds of picoseconds to about a nanosecond depending on plasma size [11].

The neutron yield is estimated using the following relation:

$$N = \int n^2 \langle \sigma v \rangle dV d\tau$$

The integral is over both volume and confinement time. For the DD reaction, the factor of n^2 appears since the reactants are both deuterons. The product $\langle \sigma v \rangle$ is a strong function of the ion temperature for the DD reactions. This ion temperature produced by the Coulomb explosions varies with laser intensity and cluster size [3]. Higher ion temperatures are strongly preferable for maximizing the fusion reaction rate. Assuming $\langle \sigma v \rangle$ and density are determined by the laser and cluster jet, increasing the plasma confinement time at a given volume will increase the number of reactions linearly.

In order to understand the effects of a radially confining magnetic field, we may model the plasma as cylindrical where both radius and length are functions of time. Neutron yield becomes proportional to the following integral:

$$N \sim \int \frac{dt}{R(t)^2 L(t)}$$

Where R is the radius and L is the plasma length, and we hold the number of particles fixed in the given volume. Take $R(t) = R_0 + v_r t$ and $L(t) = L_0 + v_z t$. Without a magnetic field, both velocities would be about the sound speed. The magnetic field should have the effect of making $v_r = 0$ so that the integral only needs to be performed over L(t). The plasma is still entirely unconfined axially. The result of the integral is a logarithm in L with R constant:

$$N \sim \frac{1}{c_s R_0^2} \ln \left[\frac{L_0 + c_s \tau}{L_0} \right]$$

This gives a neutron yield which would be a factor of L/R times better than an unconfined plasma, for which the yield is proportional to $1/c_s R_0 L_0$. This simplified model says the plasma confinement time in a strong field becomes the axial ion travel time, which is a few nanoseconds [20].

The relative effectiveness of a magnetic field depends on the plasma geometry. If the plasma axial length is significantly greater than its radius, the magnetic field should have a larger relative impact on confinement time and neutron yield [21]. For a 100 μm radius, 5 mm plasma filament, the neutron yield gain from a magnetic field would be approximately 20-50 by this estimate. For a 1 mm radius plasma of similar length, the gain would be a factor of 5 or less [6] [11].

In unconfined cluster fusion, the temperature-dependent reaction rate decreases as the plasma expands and cools. Higher reaction rate over the course of the plasma life may improve

neutron yield beyond these estimates above [6]. Additionally, if mirror trapping succeeds in preventing axial escape for times approaching 10ns, the neutron yield may be significantly improved over the above calculation [7] [8].

Modeling plasmas with initial density up to 10^{18} cm^{-3} , researchers at the Technical University of Crete predicted up to 10^9 neutrons per shot, compared to 10^6 neutrons per shot without a field. They modeled successful mirror trapping and multiple ion bounces [7] [8]. Initially denser plasma may boost the gain further than these calculations show. They do not describe or predict what effect mirror instabilities such as the interchange or the loss cone instabilities will have.

A magnetic field is expected to decrease the beam-target contribution to the fusion yield. The magnetic field should slow the radial expansion of ions and drive most of them out axially, preventing them from interacting with as much background gas and plasma [11]. The effect of this is expected to be significant, as beam-target neutrons are believed to be responsible for 40-60% of the neutron yield [11].

One caveat about magnetic confinement is that the Larmor radius of the ions, given by:

$$r_l = \frac{m v}{B e}$$

is on the order of 100 μm for a megagauss field and temperatures $\sim 10 \text{ keV}$. This is similar to the plasma radius if close to the best focus of the GHOST or Texas Petawatt Lasers [6]. This implies that magnetic confinement of the ions is limited. However, the ions may be electrostatically confined by the hot electrons. The fusion products would be able to escape the plasma, since their Larmor radius is several millimeters [20]. The relative importance of electrostatic confinement and ion magnetic confinement may be less important for radially larger plasmas, as on the Texas Petawatt away from best focus.

2.3 Magnetic Field Driver Requirements

Confining the hot, dense plasmas produced in cluster fusion requires a very large magnetic field. Magnetic pressure must balance plasma thermal pressure for beta equal to one, otherwise the plasma will expand, the density and temperature will drop, and reactions will slow or halt [6].

$$\beta = \frac{2nkT\mu_0}{B^2}$$

For $kT = 10 \text{ keV}$ and densities of 10^{19} cm^{-3} , a $\beta = 1$ plasma would require a magnetic field of 200 T. A plasma with lower temperature or density would have slightly more lax requirements; see figure 2.2. For magnetic fields insufficient to achieve beta equal to one, the plasma should expand until the density produces a pressure balance, which should still produce a measurable yield increase [6]. Regardless, it will require fields approaching a Megagauss (100 Tesla) or more for appreciable radial confinement occur. These fields are only obtainable through pulsed power apparatus [22].

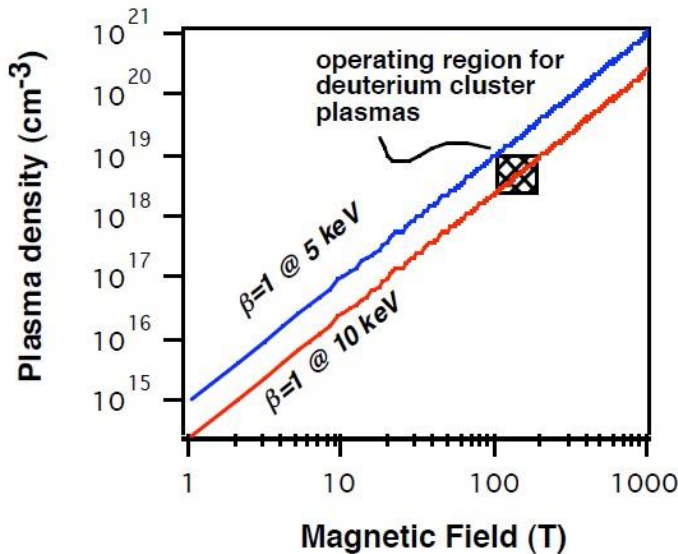


Figure 2.2: Contours of beta showing the magnetic fields required for confinement of cluster fusion plasmas. Plot by Todd Ditmire.

2.4 Context for Megagauss Field Drivers; Other Facilities

While a large number of facilities operate reusable water-cooled or superconducting magnet facilities with fields approaching 90 Tesla, it is difficult to produce fields much beyond 100 Tesla. Tremendous pressures and resistive heating from fields in this range force coils to be destructive apparatus. Megagauss fields produce pressures over 4 GPa. No material can survive these stresses [23]. For this reason, field coils must be simple and cheap. Manufacturing and replacing the coil after each shot is standard practice. This has led to the evolution of the so-called “single-turn” coil facilities, which can produce fields approaching 300 T [23]. The highest available fields available from these coils are limited by coil expansion velocity. Expansion velocity is limited only by the inertial mass of the coil, since under these pressures material strength matters little. Significant coil expansion occurs on the timescale of microseconds. Sufficient current for megagauss fields are delivered to the load in microsecond time scales before significant coil expansion occurs [23]. Fortunately for laser-plasma experiments, these time scales are much longer than the experimental timescale requirements.

The single-turn coil driven by a several hundred kilo Joule capacitor bank is the field driver configuration of choice for these laser plasma experiments. The plasma volume is only a few cubic millimeters, so a cubic centimeter so field volume is sufficient. This makes a single turn coil with a diameter of about a centimeter ideal for this application [22].

Beyond destructive single-turn coils, magnetic flux compression can produce fields of greater 300 T. These devices compress a seed field by imploding a conducting cylindrical wall containing a seed field [23]. While this method produces fields over 1000 T, the destructive nature of flux compression devices is not suited for this experiment.

As of 2003 there were 3 high magnetic coil facilities in the world that produce fields in

the desired megagauss range for laser plasma physics [23]. Humboldt University in Berlin operates a megagauss single-turn facility, the first such laboratory in Europe. They have achieved fields of over 300 T with a 200 kJ Capacitor bank and 60 kV charge voltage, although they regularly carry out experiments around 200 T [23]. Sandia's design of the megagauss apparatus presently at UT owes greatly to the work of Portugall, Herlach et al. [24] [25]. Germany has a second high magnetic field laboratory. The Dresden High Magnetic field Laboratory has specialized in longer-pulse duration fields in larger volumes with higher energies. However, they are approaching megagauss capability. Their research is focused on materials science research [26].

The National High Field Laboratory at Los Alamos National Laboratories is the United States leader in high magnetic field technology [23]. They operate a single-turn facility currently involved in condensed matter experiments led by of Charles Mielke, Dwight Rickel, and Stefan Hansel. The design of this facility also heavily influenced our setup [22] [27].

Japan has a long standing high field lab at the University of Tokyo (Kashiwa campus) and they operate the largest indoor facility in the world. For many years they focused on electromagnetic flux compression, but they also operate a single-turn coil facility with a 200 kJ capacitor bank and 50 kV operating voltage. Materials science experiments are cryo-cooled and examined with a variety of diagnostics including optical probing [23].

High magnetic field drivers for plasma physics and HEDP research also exist. The University of Rochester operates a pulsed destructible coil for laser fusion experiments capable of achieving approximately 10 Tesla. One of their primary focuses is studying the effects of field effects on transport and magnetic flux compression for ICF research [28].

Our application for cluster fusion and plasma physics requires a portable magnetic field

driver which is deliverable to high power laser facilities. The laser must operate in a vacuum so the magnetic field must also be in vacuum. The combination of these requirements is a novel technical hurdle that few other facilities have not needed to incorporate. Sandia's approach to this problem has been to design a portable vacuum chamber. We have mounted the capacitors on carts and all other electronics are on wheeled racks. The vacuum interface for the transmission lines are designed after the highly successful Z facility at Sandia [22] [29].

Chapter 3: Basic Megagauss System Design

3.1 Experimental setup

The experimental hardware includes the laser hardware, optical diagnostics, target chamber, and pulsed-power hardware. We will introduce the other hardware here, and afterward focus on the pulsed power driver for the containment field.

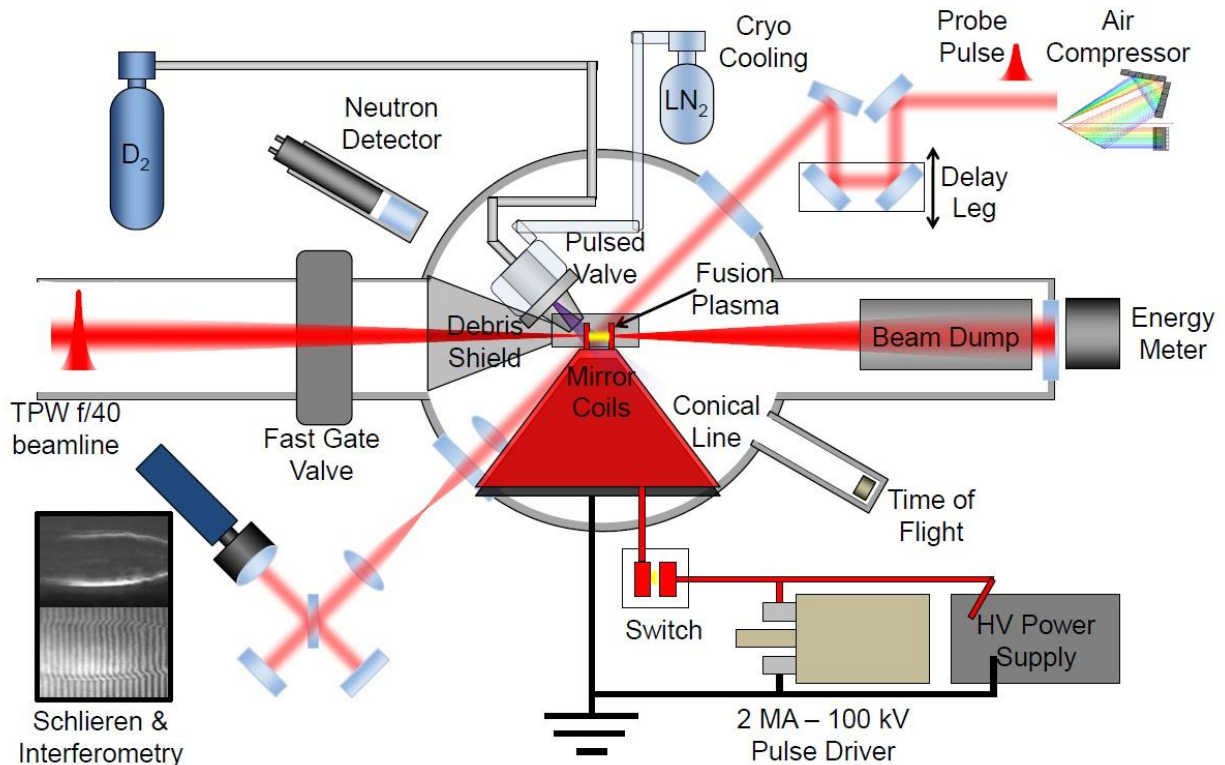


Figure 3.1 Schematic of the basic experimental setup proposed. Diagnostics including neutron detectors and transverse-beam diagnostics must be combined with the pump laser, and the pulsed power supply. Diagram by Hernan Quevedo at the University of Texas.

First, the laser target is the cluster jet supplied described in chapter 1. Clusters form in the region in the center of the coil.

The pump laser will either be the 2 J GHOST laser for early experiments or the 150 J Texas Petawatt Laser for the ultimate experiment. These lasers have pulse durations on the order of 100 fs [15]. Energy meters will measure laser beam absorption by the cluster target.

Plastic scintillators placed at least a meter from the vacuum chamber measure neutron yield and time of flight relative to the pump pulse. Deuterium ion time of flight can be deduced from Faraday Cup measurements if they have direct vacuum line of sight with the plasma, which might be experimentally difficult but useful if it can be done [6].

Additionally, there will be a series of diagnostics including a diagnostic laser beam line. This diagnostic will run through the center of the coil and across the plasma, and two ports in the chamber accommodate it. This diagnostic axis will enable transverse interferometry imaging of the plasma as it evolves in time [6].

The timing of the various aspects of the experiment reflects a hierarchy of timescales. The gas jet pulse occurs on millisecond timescales and opens before the pulsed power hardware is discharged. The pulsed power operates on microsecond time scales, while the laser fires in about one hundred femtoseconds during the peak of the current pulse in each field coil. The plasma duration should be on timescales of hundreds of picoseconds alone or up to nanoseconds for confined plasma. Figure 3.2 describes these timescales and their relation to each other.

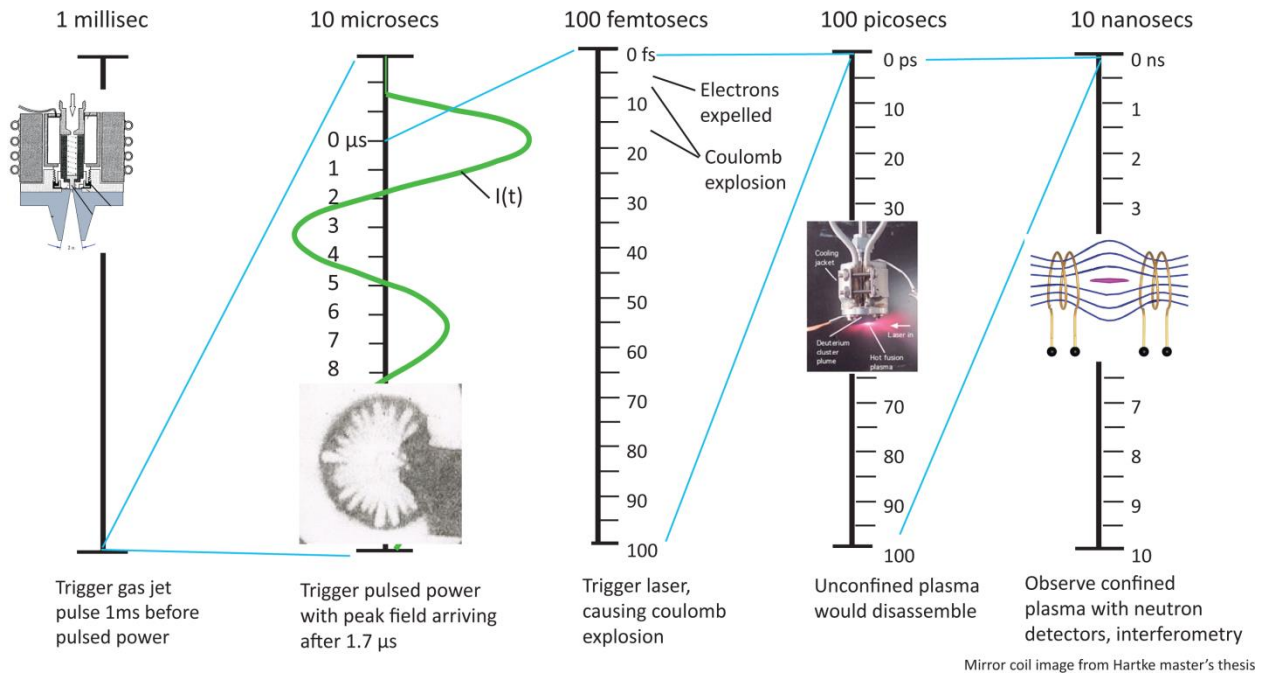


Figure 3.2 Schematic of chronology and timescales involved in the experiment. Relevant events span more than 11 orders of magnitude in timescales. Pulsed power current changes on the microsecond timescale, and this is also the timescale for coil fragmentation. Show here is an X-ray backlit image of a coil exploding after 6 microseconds [23]. Other images are relevant to cluster fusion [11]. The mirror coil confinement image is borrowed from Rene Hartke's MA thesis (2004).

3.2 Driver Requirements Restated

The pulsed power driver for our experimental needs must deliver currents of up to 2 MA on timescales of microseconds. These requirements are explained in the previous section as necessary for delivering a magnetic field capable of sufficient plasma confinement. Sandia National Laboratories, in collaboration with the University of Texas, designed and built the hardware for the pulsed power driver based largely on previously successful single-turn megagauss magnetic field drivers [22]. Additional requirements originate from working with the laser systems, which require the driver to be both portable and vacuum compatible. The system must deliver the pulsed power into a vacuum chamber, and all apparatus must be transportable to a large laser facility [22].

3.3 Upgrade to Full Current 10-Capacitor System

Originally the prototype system only had 2 capacitors operational in 2009. This smaller system was used for tests and as a demonstration of the technology [30]. The system was scaled up by a factor of 5 in capacitance and energy by going from 2 capacitors to 10. Struve set a design target of a 200 Tesla field in a Helmholtz coil geometry with a diameter of 1 cm. This requires a current of 2.2 MA, which can be delivered with 10 modules charged to nearly their maximum rated voltage of 80 kV [22].

In order for the 10-capacitor system to be fully independent from the previous system, all new hardware was constructed except for the vacuum chamber, which was retained. The hardware details will be discussed in detail in the next section, with focus on basic circuit elements.



Figure 3.3 The completed 10 capacitor system at UT, showing all the cables and switch can assemblies connected to the target chamber. The control rack is in the background on the left. This setup was used to test the system for magnetic field production.

3.4 Basic RLC Circuit

The current driver can be described as a simple RLC circuit. The capacitors are charged to a given voltage and discharged all at once. The differential equation for current as a function of time without a forcing function is given by:

$$i(t) + \frac{L}{R} \frac{di}{dt} + \frac{1}{RC} \int_0^{t=\tau} i(\tau) d\tau = 0$$

This differential equation has a boundary condition such that $i(0) = 0$, since the initial current is

0. The circuit parameters are such that the current rings down with an exponentially decaying oscillator in the under-damped case [22]. The solution for the current as function of time is:

$$i(t) = V_0 \sqrt{\frac{L}{C}} e^{-\frac{itR}{2L}} \text{Sin}(\omega t)$$

Where the oscillation frequency is given by

$$\omega = \sqrt{\frac{1}{LC} - \left(\frac{2L}{R}\right)^{-2}}$$

Pulsed power engineering was utilized to ensure the highest capacitance and lowest inductance, thus ensuring the highest peak current. The peak current is given approximately by:

$$I_p \cong V_0 \sqrt{C/L}$$

and it scales linearly with voltage and inversely with the square root of the inductance [22]. This approximation ignores impedance from the resistance in the circuit, which is much smaller than impedance from reactive components.

3.5 Capacitance

The energy for the current pulse is stored in a bank of 3.1 μF General Atomics high energy capacitors. These are microfilm stack capacitors, series C, part number 32424. Ten in parallel produce a total capacitance of 31 μF for the bank. Each capacitor is rated up to 100kV for a maximum energy of 15 kJ per capacitor. The bank total energy is 150kJ at 100kV charge voltage, however for most shots where it is desirable to avoid damaging hardware 50 kV (or less) is the preferred charge voltage and the operating energy is about 39 kJ [27].

3.6 Inductance

Inductance in the circuit limits the maximum achievable current and extends the pulse

duration. Limiting the inductance is often the most difficult aspect of pulsed power engineering, and in this case it is achieved through several means. The majority of the inductance in the circuit comes from the coaxial cable transmission lines and the switches combined with their switch can assemblies. Six transmission line cables per capacitor were used in order to keep inductance low [22].

The spark gap switches are large source of inductance also. Because the spark gap arc channel itself is so narrow, the inductance it creates is significant, usually on the order of 10 nH per centimeter of breakdown distance [31]. The design engineers considered several spark gap switches from L3 Pulsed Sciences, and finally selected the Pulsed Sciences 43650 Spark Gap switch for its compact, low inductance qualities [22].

The remaining sources of inductance are the tri-plate transmission lines in the chamber and the coil itself, which contribute about 15 nH total [27].

	Capacitor	Switch	Cables	Insulator and connection	Vacuum Line	Coil	Total
Per Line	40	70	148	1.5	3.7	5	268
Two-capacitor system	20	35	74	1.5	3.7	5	139
Ten-capacitor system	4	7	15	0.8	5.7	5	38

Table 3.1 Theoretically expected inductances in the system, including a comparison with a 2-capacitor setup and a 10-capacitor setup [27]. Units are nano Henrys.

C of bank (μF)	3.1
Vmax charge (kV)	85.0
L capacitor (nH)	40.0
L switch (nH)	70.0
R series ($\text{m}\Omega$)	100.0
Z cable (Ω)	59.0
Number of cables	6
Cable length (ns)	15.0
L connection ring (nH)	0.4
R shunt (Ω)	0.5
L insulator (nH)	0.2
L vacuum flare (nH)	0.2
L transmission line (nH)	6.0
L coil (nH)	5.0

Table 3.2 Expected circuit parameters used in circuit code simulations [27]. Most of these estimates are very close to their experimental value, although the system has a higher inductance than anticipated, closer to 50 nH. The shunt resistor has not been used for experiments.

3.7 Resistance

The resistance is dominated by the 0.1 Ohm water resistors which are located in the switch cans of each capacitor assembly. The resistance was chosen to reduce reverse-voltage swing during RLC ring-down to less than half the peak value but still deliver significant energy to the load. This measure protects the capacitors from damage. The impedance of the circuit is still dominated by the inductance [27].

3.8 Practical System Capabilities

With 10 capacitor modules, the system has a theoretical maximum current of 2.2 MA. 2.2 MA operation uses of a voltage of 80 kV at 80% of capacitor's rated maximum charge voltage.

Although the capacitors are rated for 100 kV and the cables have a DC rating of 150 kV, in practice the switches have shown limited reliability at holding off 100 kV of charge voltage. Sandia tests demonstrated that the Titan switches can pass over 200 kA, but they are only rated for 100 kA, which corresponds to a 50 kV charge voltage. Also, the chamber transmission lines are unable to hold off breakdown in atmosphere at 80 kV with a coil inductive load and 10 capacitors operating. So, although 80 to 100 kV is the maximum range, we prefer a safer mode of operation at 50 kV. At 50 nH, the impedance is such that the system delivers on average about 1.0 MA of current to a coil load at 50 kV. At 50 kV the stored capacitor energy is 39 kJ. In this mode, for a 10 nH coil, the magnetic energy in the coil is 8 kJ.

At a charging current of 30 mA into 10 modules, the capacitors take about a minute to charge. For nondestructive targets, this limits the rep rate of the system to a few minutes. Usually coil replacement after destructive shots is the primary rep rate constraint.

3.9 Low Current Mode of Operation

Several modes of operation exist for the 10-capacitor megagauss system. It can be used at

full destructive currents in which the coil will be destroyed, but the system can also be scaled down and still discharge reliably.

As explained before, one can easily control the current to the coil by altering the charge voltage. However, the switches and triggering system do not behave well for voltages much below 20 kV. The trigger signal from the Maxwell trigger generator (described in section 4.3) is about 30 kV, so the breakdown mechanism in the Titan switches does not work as intended for capacitor charge voltages this low. This means that 20 or 30 kV is the practical limit for reliably discharging the all switches synchronously, and we have seen this in practice.

Removing some of the capacitor modules from the circuit is the best way to reduce the current below 600 kA. To do this on a capacitor module, first disconnect the corresponding discharge cables from the vacuum chamber. Then disconnect both the trigger and charge cables at the trigger box and relay tank, respectively. These unconnected capacitors sit harmlessly unattached to the main circuit while the connected capacitors can still operate normally. This way, the system performs reliably at currents below 700 kA while still operating in the ideal voltage range between 30 and 60 kV.

Chapter 4: Full-Current System Hardware Specifics and Controls

4.1 Switch Can Assemblies

Sitting atop each capacitor is a cylindrical aluminum enclosure surrounding the capacitor head, spark gap switches, water resistor, and discharge cable connections. This enclosure, known as the “switch can assembly”, provides a return current path to the grounded wall of the capacitor.

The entire switch can assembly is filled with gas to prevent electrical breakdown. Originally two psig of sulfur hexafluoride was used [32]. Sulfur hexafluoride is an extremely effective at preventing breakdown as the abundance of fluorine atoms acts to absorb stray electrons [33]. In the first incarnation of the system, there was a vacuum pump intended to remove the atmospheric gasses including water vapor before inserting the SF₆. However, this did not turn out to be necessary in practice, so the 10-capacitor system did not incorporate a vacuum system for emptying the cans. When the 10-capacitor system was being constructed, 2 psig of SF₆ was used in all 10 switch cans. However, these switch cans leaked the expensive SF₆ gas at an alarming rate. These cans are not pressure rated for much more than two atmospheres or 15 psi. To save money, we tested dry nitrogen at 5-8 psig. We found that it permits arcing through the walls of the switch cans. This means that mixing in SF₆ is essential. For most shots now, the standard gas content of the switch cans is a mixture of dry N₂ and SF₆ gasses, with about 10-20% SF₆ by volume. These gases are added to the already present atmospheric gasses in the cans. If desired, the old gas can be flushed out by leaving the vents to the can volume open and running N₂, but this is not necessary with 50 kV operation.

A trigger cable and a charge cable enter the sides of each switch can. Both are 59 Ω 2121 coaxial cables from Dielectric Sciences [27]. The charging cable supplies DC voltage directly to the terminal head of the capacitor from the relay tank.

Above each switch is a water resistor in series with the switch. This is an electrolytic solution of salt water with a resistance of about 0.1 Ω . It ensures that energy dissipates in a safe way during the under-damped RLC ring-down of the current [27]. The resistance ensures that the negative-voltage swing during the RLC ring-down is approximately half of the full voltage. The 6 discharge cables connect directly to the top of this resistor with banana connectors. The cables connect to the load and are the only connection between capacitors. As a safety mechanism, the cable inductance ensures that if a short develops in one switch can, only the energy of that corresponding capacitor is discharged there [27].

The charge cable connects directly to the capacitor head. The charge cables have varying length depending on the capacitor module, and originate from the resistor network in the charging and relay tank. The charge cables plug directly into the capacitor heads with banana plugs.

The trigger cables are also 2121 coaxial cables. They supply a grounding pulse to a 1 k Ω water resistor inside each switch can assembly, visible in figure 4.3. This ‘trigger resistor’ resides between the walls and the switch can and connects to the trigger pin of each switch. These water resistors plug into the trigger pins of the switches themselves on one side and to the central conductor of the trigger pin on the other side.

The switch cans also have a safety mechanism built into them that normally grounds the capacitors directly with a shorting lever. These levers are spring activated so that they would normally be grounded when left alone. In order for the capacitors to operate, this shorting lever

must be retracted manually by the user and held in place via prominently marked pins. These pins are red handled and flagged so the user is aware that the system may be charged.

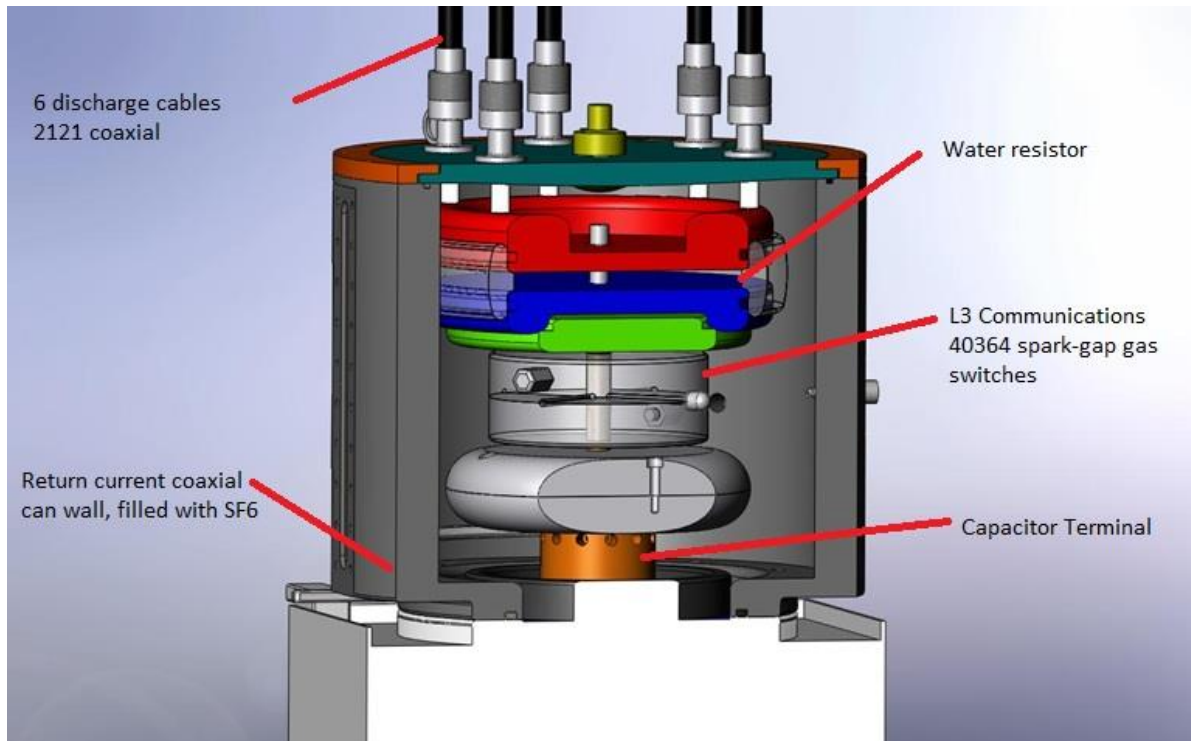


Figure 4.1 This blowout diagram depicts the most important components of the switch can assembly. Not shown are the input charge and trigger cables, and the gas pressure feeds to the switch and enclosure. Adapted from a Solidworks™ model [22].

4.2 Switches

Sandia originally tested two electronically triggered switches for this experiment. The final design incorporated a switch is L-3 Pulse Sciences Titan 40364 spark-gap switch in each capacitor module. These spark-gap switches are rated to currents of 100kA each. However, for limited use they have been tested to much higher currents exceeding 200kA, which they would need to do in this experiment. They are triggered when a sudden swing in potential on the central trigger plate creates a field sufficient for Paschen breakdown between the charged plate at the bottom of the switch, which is connected directly to the charged capacitor head, and the trigger

plate.

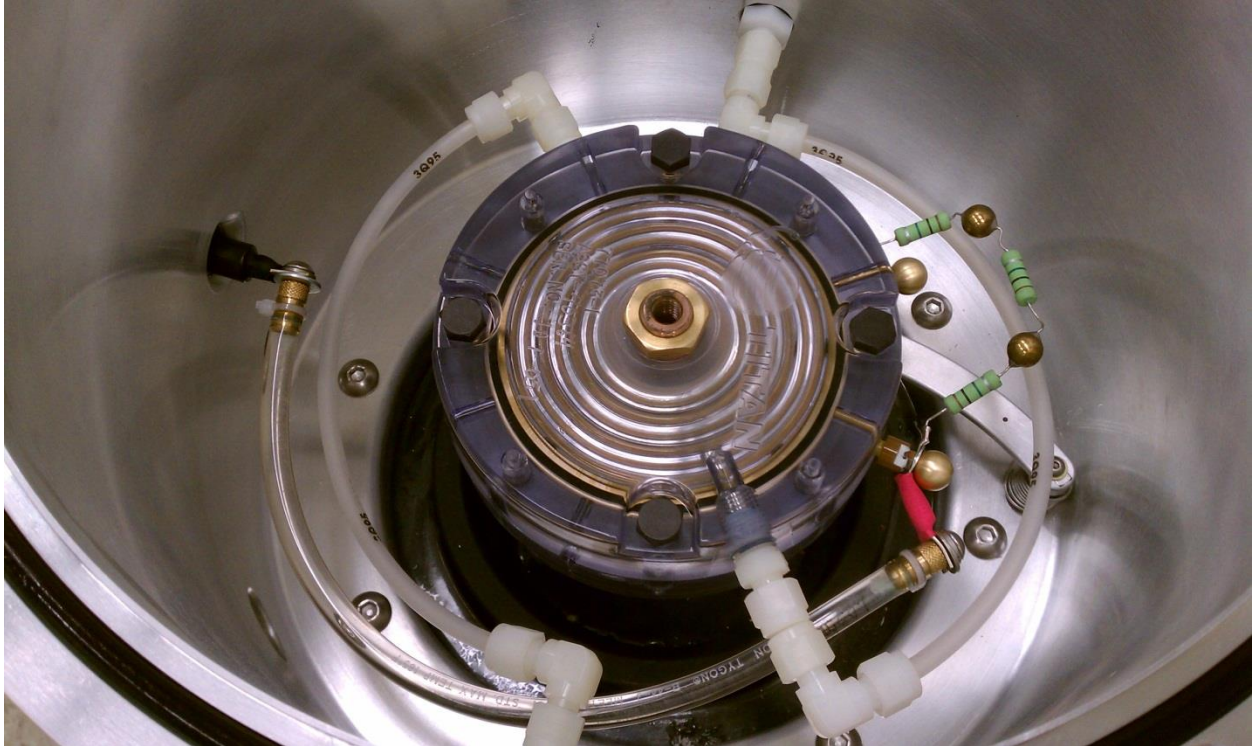


Figure 4.2 This image shows a disassembled switch can assembly. The central round blue object is the Titan 40364 Switch, with the current discharge coming out the top. On the left wall is the trigger input from the trigger box, which passes through the 1 k Ω thin water resistor shown here. The trigger pulse is delivered to the insulated pin on the central trigger plate of the switch. A small resistor network on the right creates a voltage difference that provides a small spark in the center, which is a source of UV that helps trigger the switch. Air lines come in from the top and bottom. Tubing is made as long as possible to maximize arcing paths between the switch and the can walls.

4.3 Trigger System

The system is triggered when the Maxwell trigger generator receives a 2- 30 V positive signal on the external BNC trigger input. This old off the shelf device generates a 10 ns positive pulse at 30 kV with a rise time of a few nanoseconds [25]. The Maxwell trigger generator in the electronics rack contains two trigger pulse outputs, and these two outputs went straight to the switches on each capacitor in the two-capacitor original prototype. For the upgrade, the concern was that the current from these trigger pulses would not be sufficient to trigger 10 switches on

the full-current system.

The solution was a design by Brian Stoltzfus at Sandia that used an extra “master trigger” switch to trigger all the primary switches above each capacitor. The Maxwell trigger generator triggers the master switch with a positive 30 kV pulse, and subsequently a trigger pulse is delivered to the 10 other switches on the primary storage capacitors [25]. The master trigger switch is encased in a stainless steel Hoffman box used as an oil tank, so that the switch and high voltage circuitry can be immersed in oil. The trigger box and contains inputs from the Maxwell trigger generator and a bias voltage input.

Since the trigger cables have some capacitance, they have an RC charge time. It takes about a minute for them to become charged through the 1 G Ω resistors in the switch bias. These cables must be charged so they can deliver current during a trigger pulse. Since this is comparable to the RC charge time of the big capacitors themselves, there should be plenty of time to develop sufficient charge for triggering [27].

The trigger pin on the master trigger is biased at one quarter of the charge voltage with 1 G Ω Ohmite resistors acting as a divider. This bias voltage is created inside the charging and dump relay tank and delivered to the Master trigger box on a 2121 coaxial cable. The Maxwell trigger signal itself is protected by a DC blocking capacitor from the high voltage bias that the resistor divider delivers. The spark gap distance on the master trigger switch has been decreased by a factor of two, because the master trigger operates at $\frac{1}{2}$ the voltage of the switches at each capacitor but we wanted to give it the same pressure of dry air. That this would work was verified with 2D electrostatic codes as calculated by Struve.

The trigger signal is delivered through 2121 coaxial cable to 1 k Ω water resistors inside each switch can, as mentioned earlier. This water resistor ensures a hard, fast negative swing on

the switches with residue time of order 20ns, as determined by the L/R time of the switches and the RC time of the 1 k Ω resistor.

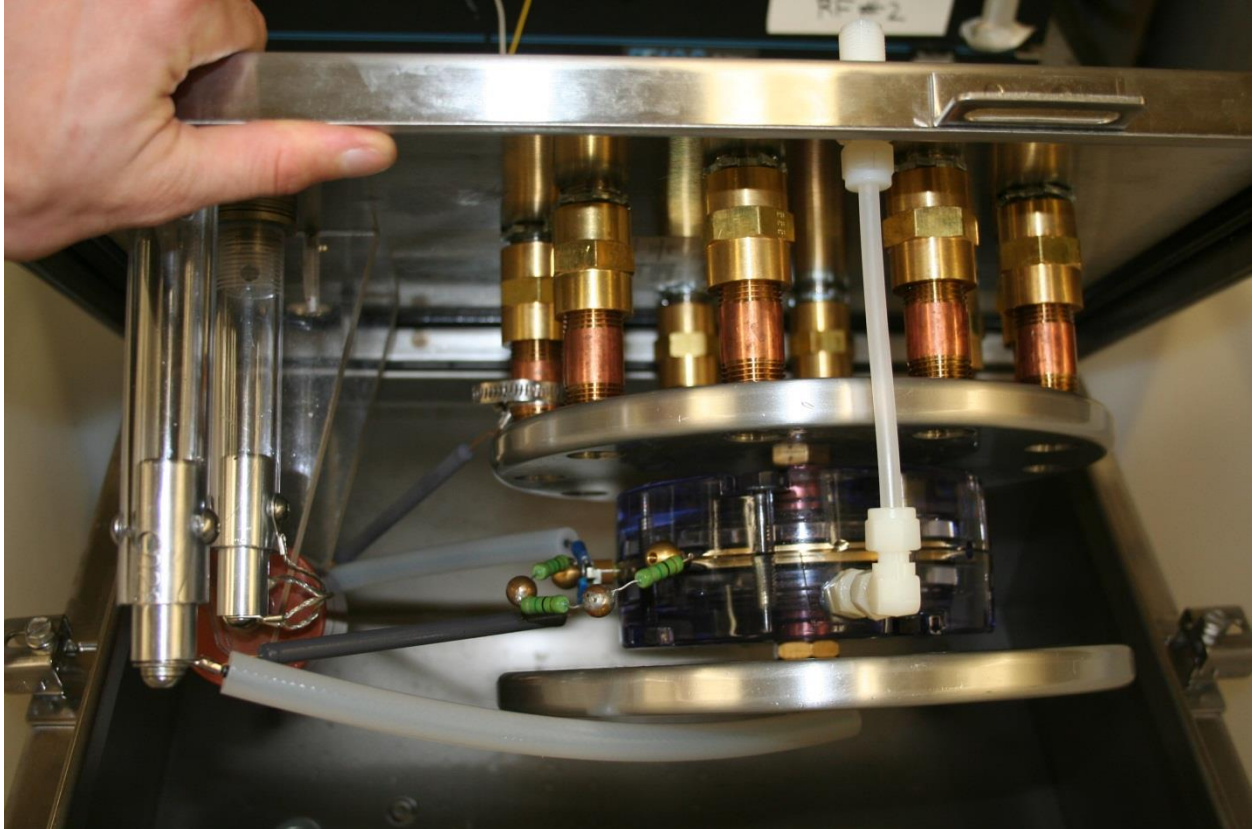


Figure 4.3 This figure shows the master trigger switch completed inside the Trigger Box tank. Each of the 10 copper pipes on top contains a trigger cable that goes to a capacitor module. They can be plugged in and unplugged at will via banana connectors on the bottom plate. The HV circuitry includes trigger plate biasing and a DC blocking capacitor for the Maxwell Trigger Generator.

4.4 Charging and Dump Relay Tank

The relay tank is a large Hoffman™ enclosure containing luminol oil for high voltage insulation. Inside is high voltage circuitry including a Ross relay capable of grounding all

capacitors safely. When the relay is closed, capacitors release charge to ground through a resistor chain in series. The Ross relay functions not only to dump unwanted capacitor charge in the event of a failed shot, but also as a safety mechanism which maintains the capacitors at ground potential until the system is ready to be used. It is controlled directly through LabVIEW™ software and should be only opened by the operator immediately before charging the capacitors for a shot. It should be closed immediately after a shot. In the event of a wall power failure or other system fault the Ross relay will also close on its own, safely dumping any charge on the capacitors.

There is also the DC supply which charges all the capacitors, which supplies voltage to one side of the series resistor network. Each energy storage capacitor is connected between resistors in the series chain. As described, these resistors protect the capacitors in case of grounding failure when the Ross relay closes. They also provide current limitation for charging the power capacitors with the Glassman supply voltage with an RC time of about 1 minute.

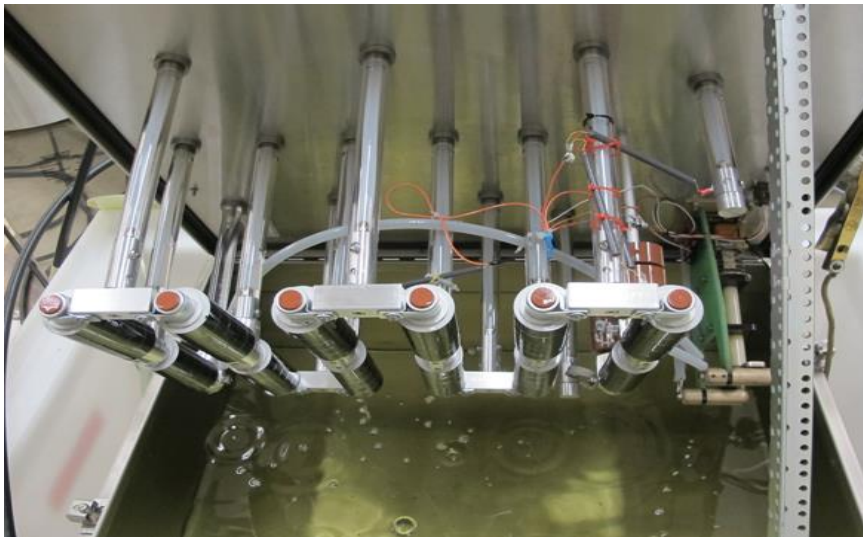


Figure 4.4 The relay tank. The array of resistors most clearly visible is the network used to deliver charge current to the capacitors. The Ross relay is the green device visible behind them.

4.5 Electronics Control Rack

The control rack [Fig. 4.5] is an enclosure containing a number of important elements, including a trigger generator and power supply. It also contains an electronics and pressure control sub-enclosure. The control rack contains the electronics necessary to control the rest of the system. It is a slightly streamlined version of a prior control rack built to control the two-capacitor prototype, which was designed and constructed by Caleb Waugh and Brian Stoltzfus at Sandia.

The control rack includes a Glassman (model PK125R30) high voltage DC power supply, which can supply up to 30 mA and up to +100 kV DC as a supply of charging voltage for the capacitors. It is controlled with a custom control cable that mates with the electronics enclosure. The charging cable is a 2121 coaxial cable that plugs into the charging and relay tank.

The Maxwell 40168 trigger generator is contained on this electronics rack also. It supplies a 30kV positive pulse to the master trigger switch. A small quantity of dry air is supplied continuously while it is operating. The Maxwell has several external safety features. Mainly a high voltage interlock is controlled by a key externally on the control rack.

Above the control rack assembly is a red warning light which becomes active when the dump relay in the Ross relay is open. If the relay is open, the capacitors no longer have a route to ground except through the coil load and thus become dangerous. This strobe light is meant to warn people in the room that the system is active and it is necessary to evacuate.

On the front of the control rack is a stainless enclosure with various control electronics. This enclosure also holds system of pressure controls designed to supply dry air at a regulated pressure to each of the 10 switches on each capacitor plus the trigger switch in the relay tank, all

in parallel. The pressure in each of these switches can be controlled electronically through LabVIEW software using an electronically controllable pressure regulator. The pressure in each of the switches is critically important because the system needs to be able to operate at different voltages, and only a narrow range of switch pressures will work appropriately at each voltage.

Glassman High Voltage Supply

Maxwell Trigger Generator

compactRIO Controller

Solenoid Valve and Regulators

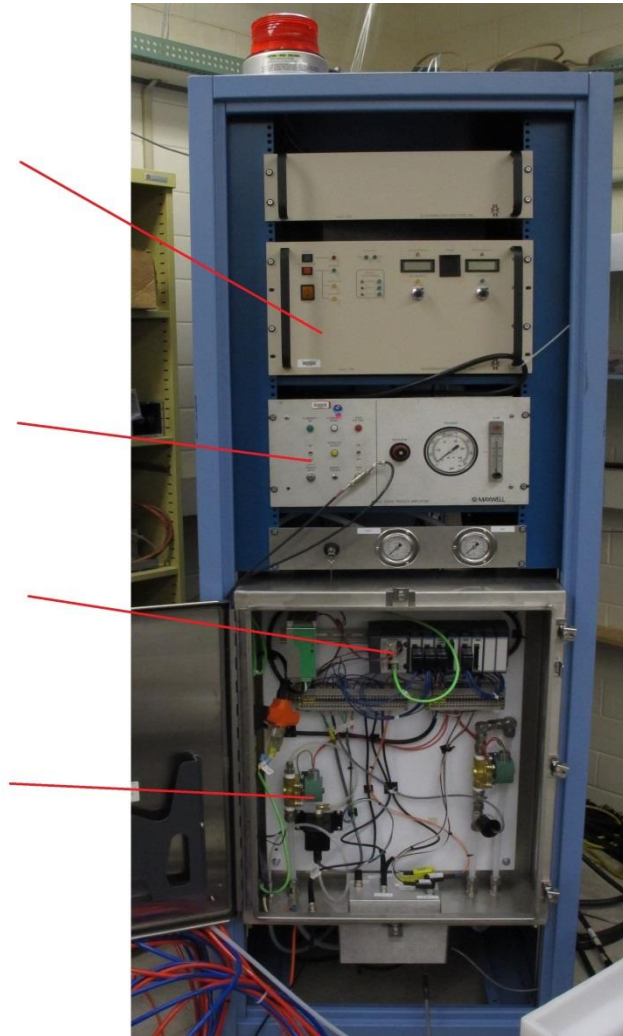


Figure 4.5 This is the electronics control rack. Featured devices include the Maxwell trigger generator, the glassman HV supply, pressure monitoring gauges, and a warning light on top. Apparatus for interacting with the control PC and managing switch pressures are in the Hoffman box on bottom.

The most important aspect of the control rack is a National Instruments CompactRIO™, (National Instruments cRIO-9012) which controls all components of the 10-capacitor system [34] [27]. This device contains I/O modules for different applications, including DC logic, AC

relays, AC power supply, and voltage sensing. It communicates via a fiber optic connection with a PC running LabVIEW™ software. The CompactRIO controls the Maxwell trigger pulse generator, the Glassman high voltage generator, the regulators and solenoid valves for dry air pressure, the dump relay, the hazard light, and the interlocks.

4.6 Voltage Sensing and B-dots

The current passing through each switch can assembly is measured with a B-dot probe in the wall of the aluminum can. The B-dot probe is just a loop of wire embedded in plastic. It detects induced voltage from the changing azimuthal magnetic field in the switch can assembly, and is measured and recorded in a bank of oscilloscopes.

The oscilloscope rack contains four oscilloscopes, as well as a network switch that communicates with these scopes, the cRIO controller in the control rack, and the control PC. These scopes acquire B-dot signals from each of the switch can assemblies, as well as from load B-dots.

The charge voltage on the capacitors is measured at two points on the top and middle of the resistor chain in the charging and relay tank. It is important to know the voltage on the capacitors at any one time during the charging process. This voltage sensing is carried out using resistor dividers configured to give a voltage signal between 1 and 5 volts from an input voltage of 10-100 kV. The output of these dividers is fed through the main control cable for the charging and relay tank, which connects to the control rack. The voltage is read directly using the compactRIO controller. When these two sensing points in the resistor charging chain are at equal potential it gives a good indication that the system is fully charged.

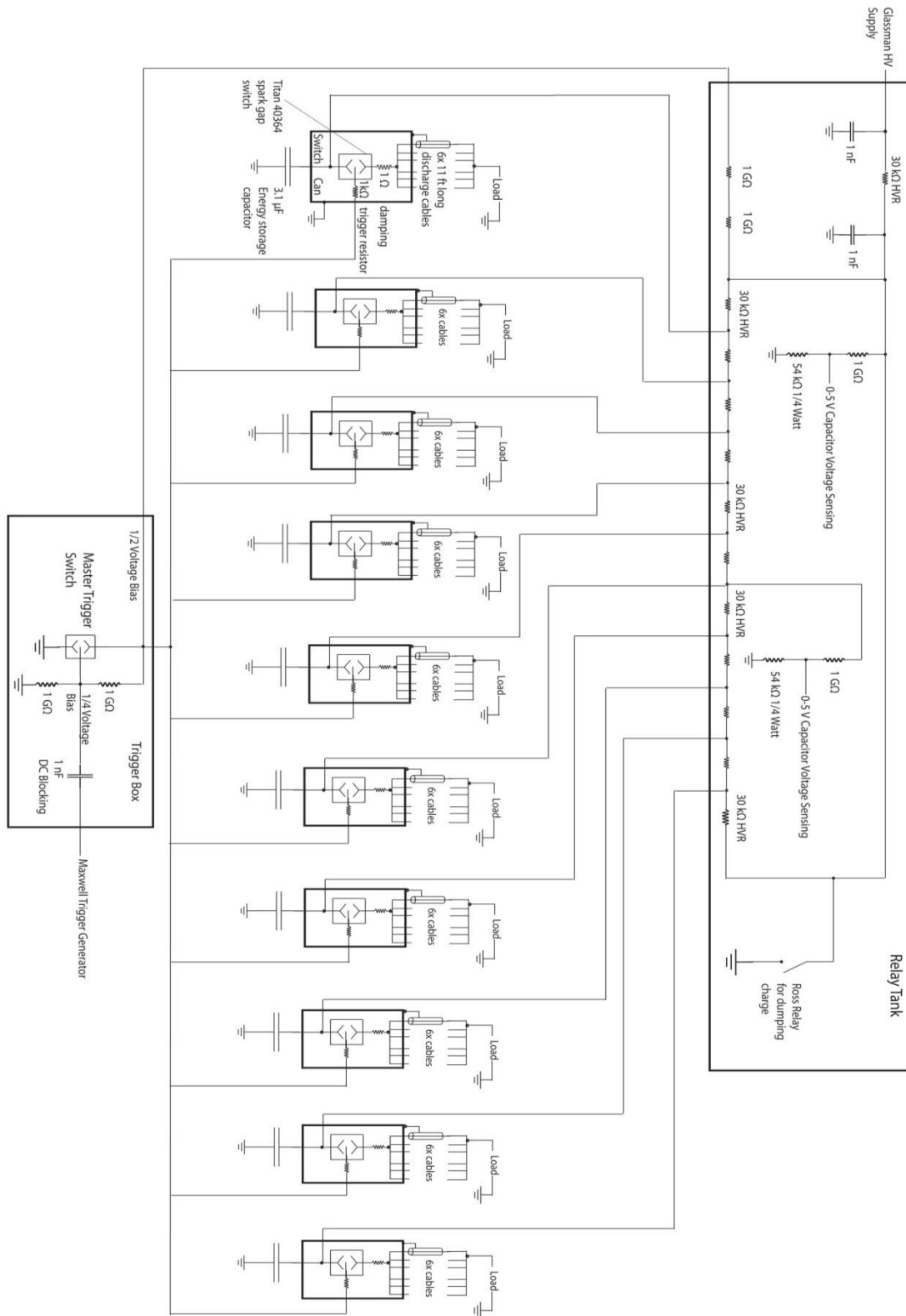


Figure 4.6 On preceding page: overall circuit diagram of Megagauss 2.0. Includes charging array, primary RLC power circuits, trigger circuitry, and voltage sensing.

4.7 Vacuum Chamber

The vacuum chamber needed to be portable and accommodate both a pump laser and a diagnostic laser beam axis. A major technical hurdle is delivering pulsed power through the vacuum interface. This is accomplished similarly to the Z Accelerator at Sandia [22]. Designers Jeff Argo, Jeff Kellogg, and Daniel Hadley settled on a tri-plate transmission line inside the chamber to deliver current to the load coil. Between these plates at the vacuum interface are a series of plastic rings and each metal plate mates to its neighbor through a plastic spacing ring and an o-ring. The current supply cables plug into metal straps that interface with the tri-plate transmission lines outside the vacuum interface. The vacuum seals because the chamber pressure clamps down on each of the o-rings between the transmission lines [22].

The transmission lines are in a tri-plate configuration, but they do not function as magnetically insulated transmission lines as on the Z-machine because the current is too low [33]. For this reason, the transmission lines are susceptible to arcing as a function of pressure in the chamber.

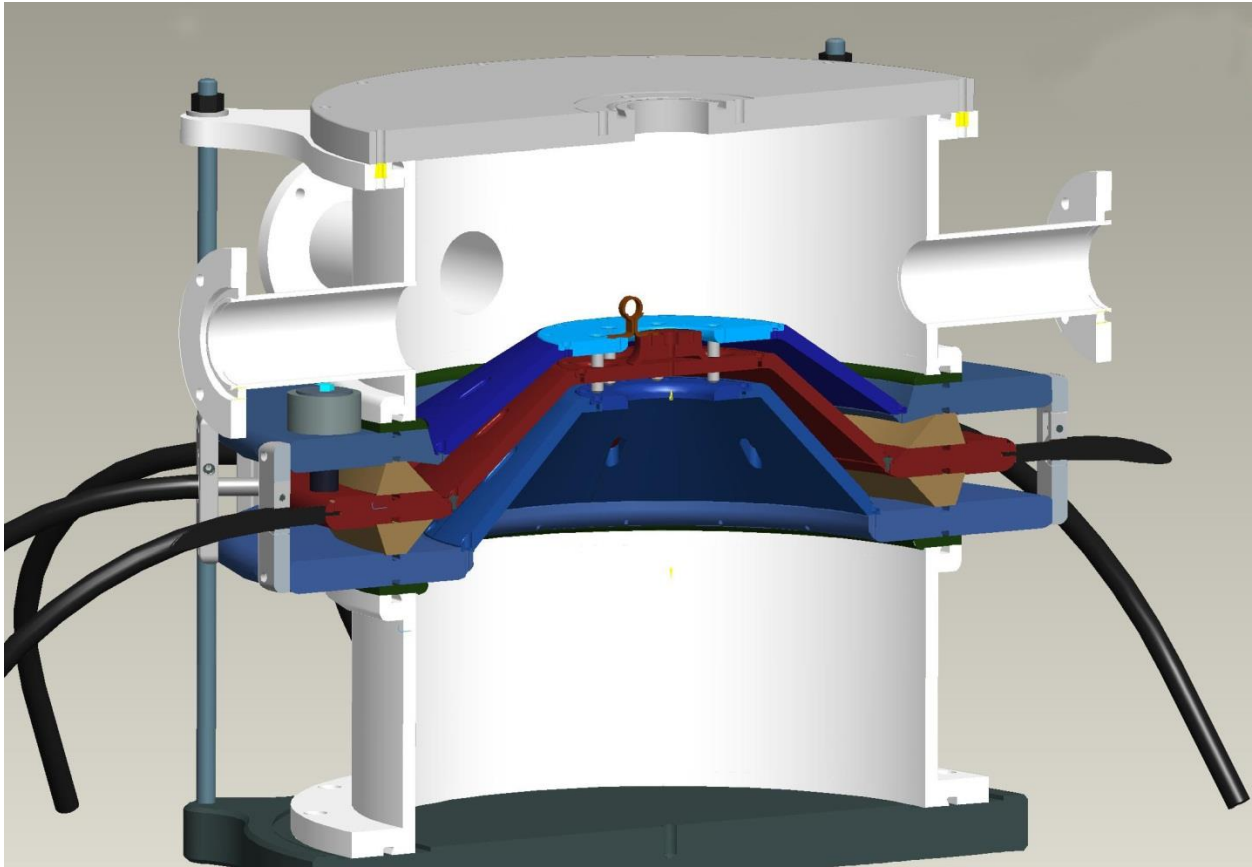


Figure 4.7 An older version of the vacuum chamber or target chamber assembly used for the Two-capacitor system. The 10 capacitor system is the same chamber but with more cable attachments. Note the two beam axes passing through and across the coil. Also note the tri-plate transmission lines used to deliver the current to the coil [27].

4.8 Modifications to the chamber for the 10-capacitor system

Modifications to the vacuum interface in the pulsed-power transmission lines were required to accommodate additional cables from 8 new capacitors in the 10-capacitor system. The outer sheaths were enclosed in a metal sleeve and clamped in place with an aluminum strap. This strap screws into the top and bottom cathode plates, while the anode plate has holes designed to accept the central conductor from the coaxial cables. In the new system, a total of 60

cables plug into the side of the vacuum chamber's tri-plate transmission lines. The outer transmission line plates had to be modified to accommodate 48 additional cables. Now the cables are closely packed together with the grounding straps fitting together tightly.

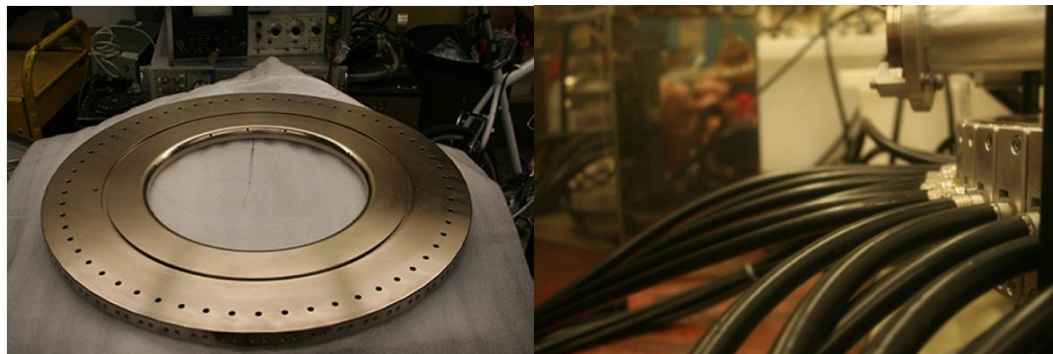


Figure 4.8 On the left is a new stainless steel cathode transmission line plate, which accommodates 60 cables. To the right, the cables have been installed in their grounding straps. The cables are as closely spaced as they can be but all 60 are able to fit around the full circumference.

4.9 Safety Measures

A handful of features are designed to protect the safety of the operators of the megagauss system. First, a set of shorting levers exists at the base of each switch can assembly. This is a spring-loaded switch lever that sits normally closed, grounding the capacitor head directly. Prior to firing, each of these shorting levers must be retracted with a set of red-handled pins. All 10 pins must be in place for any of the capacitors to charge, since the capacitors are linked in series with a resistor chain.

The Ross relay (model E60-NC-80) in the relay tank, or simply the ‘dump relay’, is a safety mechanism that provides ultimate control of whether the capacitors are grounded. It is safely grounded through a set of high voltage resistors which prevent catastrophic direct discharge of the capacitors to ground. This relay is always closed while personnel are in the

room. The hazard light on the control rack turns on as a warning that the dump relay is open and the capacitors may now be charged.

The Maxwell trigger generator has a set of enabling switches on its front panel. After it is turned on, the Maxwell has a 5 minute delay built into it before it can become active. Then an indicator light “filaments ready” turns on. The megagauss system incorporates a keyed interlock on the control rack. This interlock must be engaged before the high voltage trigger on the Maxwell can be enabled.

The standard procedure is to vacate the room when the high voltage Glassman supply and the Maxwell trigger high voltage are activated. The dump relay is opened only after personnel have left the room.

The high voltage transmission lines in the system are completely enclosed by grounded shielding, so at no time during the operation of the system is a high voltage terminal open to the surroundings. All high voltage cabling is coaxial. In general all circuit transmission carrying high voltage is enclosed in grounded containers or insulating media such as oil or SF6.

The destruction of the coil produces a large quantity of copper dust and debris. This is removed with a HEPA-filtered shop-vac each time the chamber is opened. This dust is potentially hazardous to the lungs.



Figure 4.9 The red pins used to hold and retract the grounding levers. The warning strap is labeled “grounding lever retracted”. These pins must be in place for the capacitors to be charged.

Chapter 5: Results from Megaamp Destructive Shots

5.1 Switch B-dot Calibration for the 10-capacitor System

The method for measuring current passing through each capacitor module is the B-dot in the switch can assembly. The B-dot output voltage as measured with an oscilloscope will give the time derivative of B, which can then be time integrated using MATLAB or LabVIEW software to get a magnetic field. Care must be taken to ensure proper numerical zeroing and scaling during this process [32]. The B-dots are fixed in place so once these parameters are obtained they do not need to change. Magnetic field is directly proportional to current, so the B-dot's time-integrated signal is used to measure current through each switch can and capacitor module.

These B-dot probes must be calibrated so that a specific voltage change corresponds to a known current. To do this we use a current viewing resistor, or CVR, to measure current directly. This is a high power resistor specialized for measuring large pulsed currents. For calibration, it is placed directly in the target chamber between the anode and cathode. Its voltage drop can be measured with an output voltage monitor. Since its resistance is known, the current can be measured directly. Each capacitor was tested with the CVR individually. The CRV is limited in the amount of energy that it can absorb, so low charge voltage of 30kV was chosen and each capacitor tested individually. The CRV gives a direct measurement of current as a function of time, which can compared to the integrated voltage trace from a B-dot probe for calibration. This was one of the first operations carried out on the 10-capacitor Megagauss system after it was assembled at UT [32].

5.2 Full-System Shot Tests

The first full shots carried out on the megagauss system were tests of the full system working together. The first shot was at a charge voltage of 30 kA, followed by one at 40 kA. Finally, a shot at 50kA was carried out. These initial tests were into a steel bar to act as a short between the anode and cathode. The first shot that should nominally have been a mega-amp shot was shot 3. The shorting bar load was launched from the two screws holding it by magnetic pressure, and impacted the Polyethylene debris shield plate above it, leaving an indentation.



Figure 5.1 A steel shorting bar after the first megaamp shot on the full megagauss system. Magnetic pressure launched the bar vertically, causing it to collide with the debris shield plate above it. The shorting bar itself displayed signs of pinching and heating effects.

One aspect to verify in this first round of shots was the trigger system. On the first shots, B-dot data from each of the switch can assemblies showed that each capacitor module triggered synchronously to within a few tens of nanoseconds. In some future shots, we have had one or several switches discharge early or late, but this is generally not a problem. Also to be verified was the relay tank. After correcting some problems with the software controlling the relay tank,

all operations involving charging and safely dumping charge on the capacitors were shown to work as anticipated.

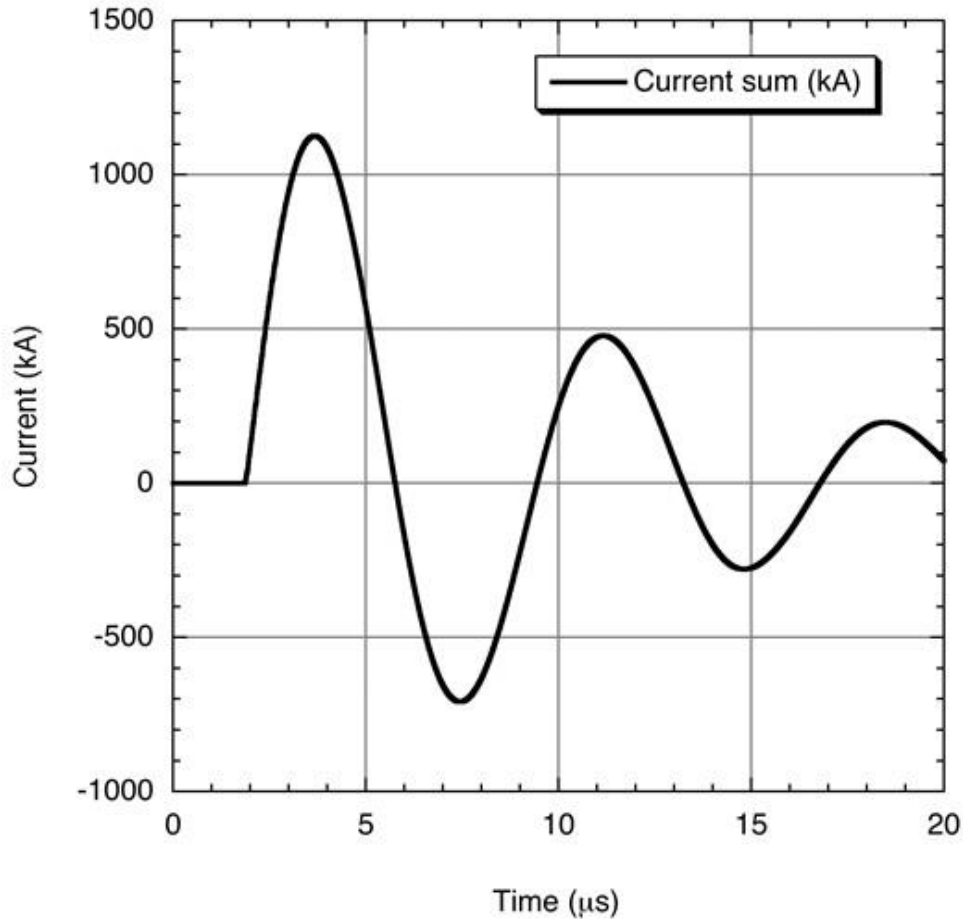


Figure 5.2 This plot shows the time behavior of the switch currents from a 1.15 MA shot. This is compiled from a sum of the integrated Switch B-dot signals. Current rise time is about 1.7 μs . Plot by Matthew Wisher in EXCEL.

5.3 Megaamp Shots with Coils in Atmosphere

The first full shots with coils verified the destructivity of currents approaching a megaamp. Megagauss shot 5 was a 50 kV shot with more than a megaamp current delivered to a

slotted coil. Most of the coil was obliterated after the shot, with many pieces thrown about the chamber along with some copper dust. The debris shield that was used for this shot experienced small aluminum craters from coil debris impacts.

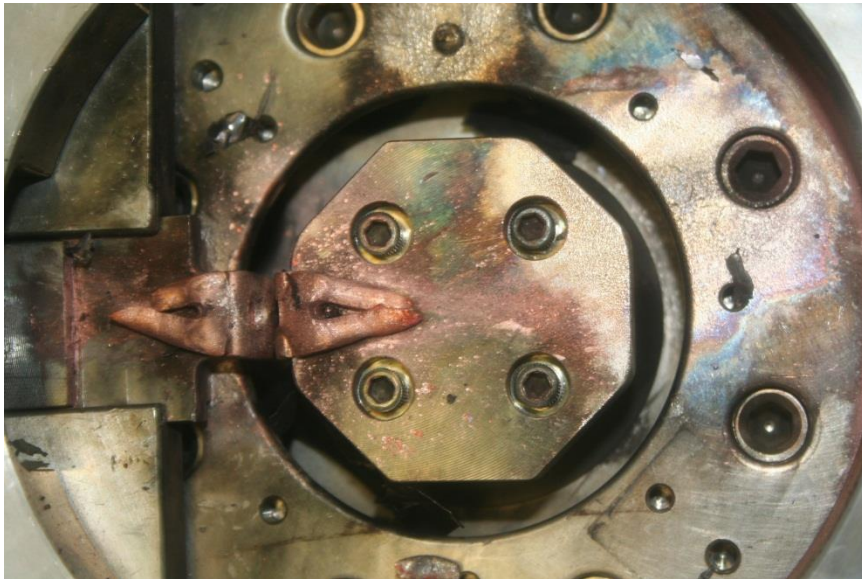


Figure 5.3 The remains of a slotted copper coil after 1.1 MA atmosphere shot #5. Note the evidence of arcing to the right between the corner of the hexagonal anode and the round cathode plate. Shot #4 produced this discharge, which afterward prompted the corners of the hexagonal plate to be filed down and eventually rounded off.

5.4 Failure Modes in Atmosphere

Several shots have demonstrated failure modes that can occur in atmosphere. These failures are typically electrical breakdowns between the transmission lines which short out the coil. Note that the coil itself only experiences a voltage drop of a few thousand volts, which is based on its inductive impedance of about 10 nH. Yet, even though this is a relatively small voltage, breakdown can occur in the vicinity of the coil, carrying the full current through a single

arc channel. It was found from these breakdown modes that the cleanliness of the transmission line region near the coil is important. The transmission lines are not insulated by anything other than about a centimeter or less of air or vacuum.

In atmosphere, the failure mode breakdown results in high heat deposition in the neighborhood of the arc, melting and deforming the metal nearby. This is evident in figure 5.4, as well as in figure 5.3. The melting and deforming often requires extensive cleaning with files, adhesive pads, and sand paper to remove the sputtered stainless steel's rough edges. In atmosphere, it is necessary to prevent burrs and other sharp edges which increase the local electric field.



Figure 5.4 The results of an arc in atmosphere on the stainless steel transmission line anode plate. Panchen breakdowns in atmosphere concentrate all the current in a single arc and are particularly catastrophic.

5.5 System Inductance Comparison to Models

The system inductance turned out to be higher than anticipated both for shots with a shorting bar and shots with a coil. Predictions were for an overall inductance of about 38 nH. This includes a tabulation of inductances as described in table 3.1 and section 3.6 [27]. The measured inductance from the sum currents on the switch B-dots indicates an inductance closer to 45 nH [27] [32]. It is unknown what accounts for this additional inductance. It may be partially explained if some of the discharge cables are not making appropriate contact and being each an extra foot longer than spec, but this would only explain a small percentage of the effect.

5.6 Vacuum Operation

The system has demonstrated a small number of destructive shots in vacuum that delivered most or all current to the coil without shorting through breakdown in the transmission lines. None have been verified with Faraday rotation to date.

The first successful 1 MA vacuum shot was shot 13. This was a 10-capacitor 50 kV shot. Shot 13 had the distinction of being carried out under careful and clean vacuum conditions although it is uncertain if this helped prevent breakdown. Finally, shot 105 was the second demonstration of full current being delivered to the load in vacuum. A long campaign of shots in late 2012 was intended to resolve vacuum arcing issues, the details of which are beyond the scope of this thesis.



Figure 5.5 An image of the coil fragments from vacuum shot 13. To the left is an identical coil prior to being shot. Many of the copper fragments had to be extracted from the aluminum wall of the chamber where they were buried from impact.

5.7 Vacuum Operation Failure Modes

The majority of megagauss shots with the target chamber under vacuum have been failures with less than the full current delivered to the coil. In the early history of the system, vacuum shots 8-12 were failures. The shots in series 31-51 were also failures to varying degrees. There have been very few since. In “failed” vacuum shots, it is likely that the bulk of the current did not pass through the coil because the coils. B-dot diagnostics placed near the coil indicate a current trace that deviates from a conventional RLC ringdown around the time of peak current, with the change in the magnetic field going to zero within 10’s of nanoseconds. In many cases the coils received less than 400kA, most likely quite a bit less. During shots 31-40, B-dot traces with the inductive loop near the coil indicate current in the coils rose usually to several hundred

kiloamps, but did not rise further, despite the B-dots in the switches indicating a full current load was delivered. This is an indication that the current bypassed the coil and flowed elsewhere, likely through vacuum breakdown. Evidence on the transmission lines show many tiny pits, dendritic streaks and in some cases molten metal debris. Many more recent shots have explored vacuum breakdown; see figure 5.6 for a representative example.

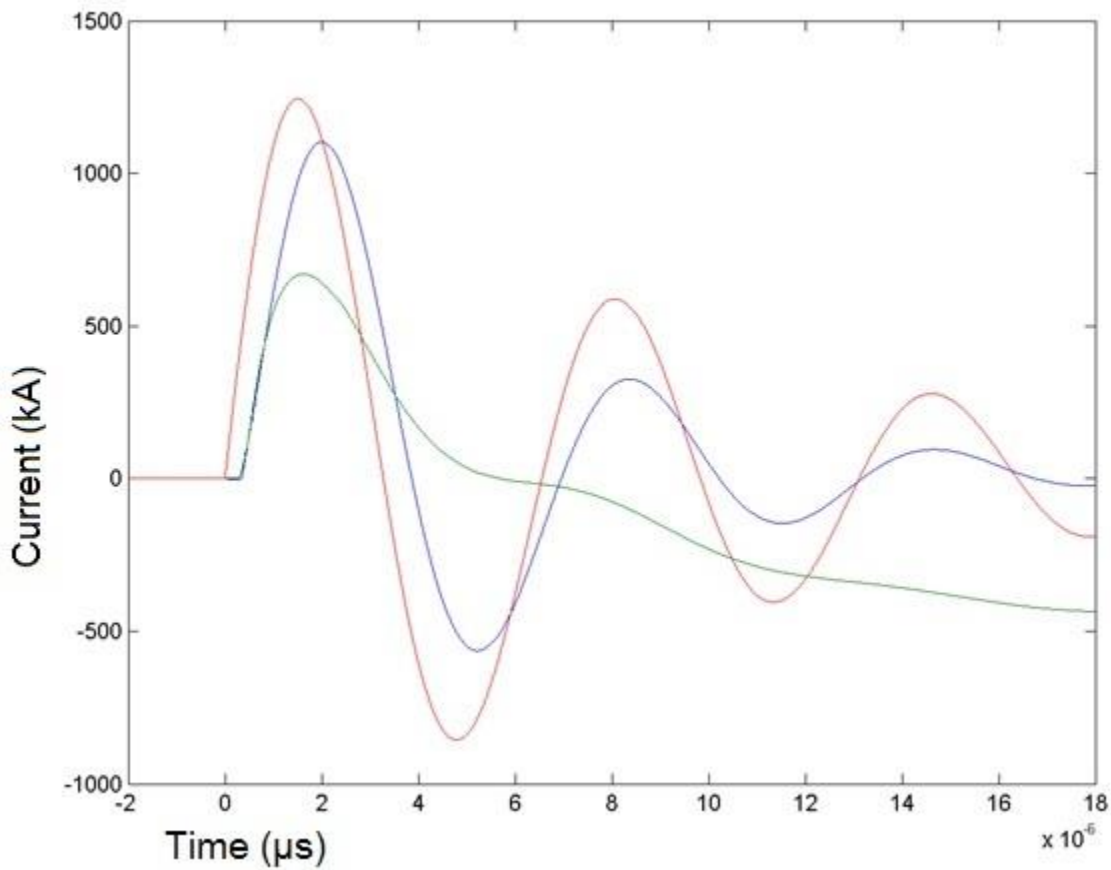


Figure 5.6 A current trace from B-dot data on failed vacuum shot #406. The green trace is the coil B-dot placed concentrically. The red trace is a theoretical under-damped RLC ring-down for a predicted system inductance. The blue trace is the sum current. The field coil B-dot indicates a breakdown after the coil achieved a current of about 600 kA. Traces are plotted in MATLAB with data parsing code written by M. Wisher.

5.8 Sensitivity of Transmission Line Breakdown to Chamber Pressure

There are a few definitive conclusions that can be drawn from vacuum shots at various pressures on the megagauss system. It seems that pressures in the milliTorr range allow breakdown easily between the transmission lines, preventing current from reaching the coil. They usually lead to breakdown before peak current. Pressures that are lower, in the 10^{-4} Torr range can allow the peak current to be delivered to the coil, but generally cause breakdown before peak current is delivered. This is based on evidence from placing a B-dot near the coil, concentric with it and several centimeters away. Insulation helps, but makes achieving low vacuum difficult. Pressures in the 10^{-5} Torr range have never been achieved.

5.9 Reduced current nondestructive shots

Shots with less than 10 capacitors included shots 52-104, carried out with only 3 capacitor modules connected to the load and a current of roughly 200kA. Shots 180-340 were 2 or 1 capacitor shots for low field tests on the GHOST laser. These tests were carried out by Wisner and Matthew McCormick at UT to measure the effects of the magnetic field on electron and plasma transport, as well as test hardware for compatibility with doing cluster fusion [32].

Chapter 6: Coil Behavior

6.1 Coils

The field coils that the experiment relies upon are based on the single-turn coils used successfully for other high field labs. These have used copper or steel material for these coils in the past, usually of 1/8th inch thickness.

Current is delivered to the feeds or legs of the coil, which are about a square centimeter in size and contact the cathode and anode plates directly. A sheet of Mylar between the coil feeds provides insulation to prevent direct current flow between the coil feeds. The inductive voltage drop across the coil using $L \frac{di}{dt}$ is on the order of a few thousand volts for a 50 kV shot [32]. The sheet of Mylar must go all the way around the inner diameter of the coil to ensure proper insulation. If the coil is shorted from arcing it prevents or stymies magnetic field formation in the coil volume. Often we observe that some of the current from the driver will be delivered to the coil as desired, but some of it will be diverted elsewhere in an unwanted breakdown in the transmission lines or coil feeds.

Coil size and density are the limiting factors for the maximum field a single-turn coil can deliver. Since material strength is marginal at the magnetic pressures under consideration, inertial confinement can be improved by thickening the coils or choosing a denser material. The conductivity of the material determines how rapidly it moves to a liquid or plasma state [23].

On the megagauss system, several different types of coils have been tested. Steel coils have been tested for one shot as a novelty, with the remainder of the shots being in copper. Copper is the material of choice for single turn coils, due to its relatively high density and high

conductivity. Slotted coils have been used frequently. Originally, the gas jet nozzle was intended to release clusters into the coil from above, with the diagnostic beam traversing through the sides of the coil, perpendicular to both the nozzle and the z-axis of the coil. For these purposes, a coil with a slot through the center was created and used for many test shots. These coils have two parallel branches. The distance between these feeds is approximately double the Helmholtz-like separation, since the total length is similar to the inner diameter. Solid coils have also been tested. The precise geometry of the coils and gas jet nozzle that will be used in our experiments is still being worked out.

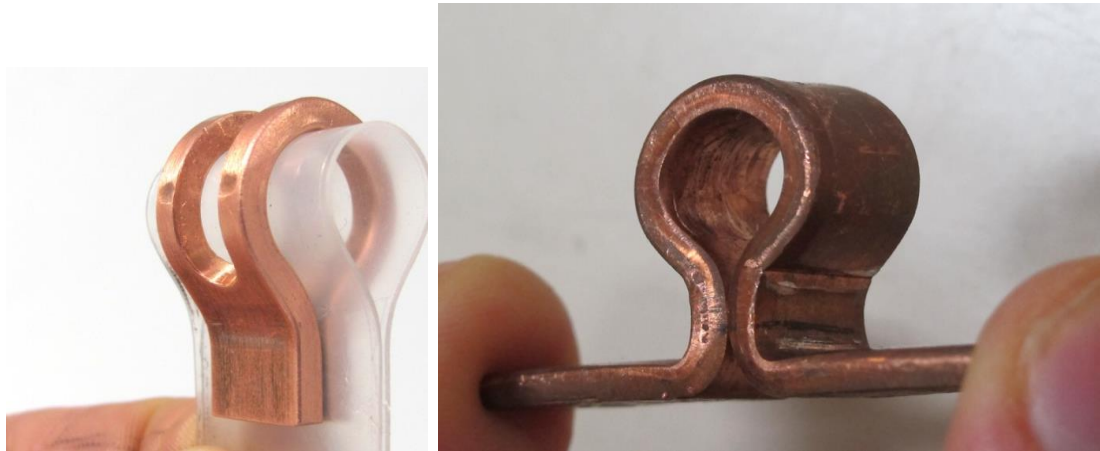


Figure 6.1 Left: slotted coil with a $\frac{1}{2}$ inch inner diameter. A Mylar sheet is placed inside the coil gap to prevent arcing. Coils of this size are no longer used, as we have moved to $\frac{3}{8}$ th inch inner diameter coils. Right: A more recent, solid coil without Mylar with an inner diameter of $\frac{3}{8}$ th inch and feeds that clamp flat on each electrode plate.

6.2 Coil Clamp

Wisher designed the coil holder used in these experiments [32]. Unlike many of the other

single turn facilities, this clamp does not use tremendous mechanical pressure to make electrical contact with the coils over a large surface area [23]. It only contacts the coil feeds with a surface area of about a square centimeter. During each shot, liquid metal bridges form as the extreme current and heating conditions grow. The magnetic pressure on the coil feeds pushes them outward. It is not known quantitatively how effective this method of current delivery to the coil is. Brass foil has been used with some success to alleviate contact welding.

The coil clamp has since seen several re-designs. One features coils with feed legs that bend 90 degrees outward. The feeds are clamped between two stainless steel sheets with bolts. This increased the contact surface area greatly and alleviates the risk of the entire coil squeezing upward from magnetic pressure.

6.3 Mechanism of Coil Explosion

The most notable effect from megaamp currents and megagauss magnetic fields is the radially outward expansion of the coil. Magnetic pressure causes the coils to explode radially outward. Coil expansion velocity ultimately places a limit on the maximum field that can be created with a single-turn coil [22] [23]. This is a result of the fact that the expansion rate of the coil increases with the square with the field and current. For a fixed volume necessary for a given experiment, increasing the current in the coil would normally be the only way to increase the field. The current is limited by RLC rise times and the inductance of the coil itself. As the size of the coil expands from magnetic pressure, the rate of expansion of the coil eventually becomes so great that increasing the current does not help. This limit is reached around 300 Tesla for a single-turn copper coil with a diameter of about a centimeter [22] [23].

An estimate for coil expansion rate and imparted velocity to coil fragments can be found by integrating magnetic pressure over an area and over time to obtain an impulse. A simple

model of the coil's inertial confinement leads to the timescales required for single turn fields. For fields of 100 Tesla, $P = B^2/2\mu_0$ gives 4 GPa. For a 3 mm thick copper coil 'sheet', the areal density is 3 g/cm^2 . We get an acceleration by dividing pressure by areal density, giving us 10^8 m/s^2 . A precise calculation would integrate magnetic pressure over a sinusoidal current. As an approximation, we can assume field durations of 500 ns, providing a final radial velocity of about 100 m/s at 100 T. Expansion velocities of a millimeter per microsecond (km/s) are obtained for typical copper coil dimensions and a field of 200 T. This expansion rate approaching the coil size is the fundamental reason that single turn coils must operate with microsecond time scale pulsed power and are limited to hundreds of Tesla.

6.4 Coil Expansion Velocity Measurement

This expansion velocity was measured with a high-speed framing camera from Sandia National Laboratories. The coils were imaged during expansion using a white light back-light provided by a flashlight and several lenses for magnification. Diffuse white light allows multi-frame images through the prism of the fast camera. The camera uses pulsed MCPs to amplify very small amounts of light over small exposure times of 10 ns or more. On most shots, the majority of the images are washed out by arcing light.

These expansion velocity experiments use the older $1/5^{\text{th}}$ current system at 220 kA. The coils had a thickness of less than a square millimeter and a length of 1 mm. Field models described in section 6.8 which assume a uniform current distribution predict a field of about 30 T in these coils, providing a magnetic pressure of 300 MPa. These thin coils have an areal density on the order of 0.5 g/cm^2 , so expansion velocity is expected to be about $\sim 50 \text{ m/s}$. The measured value was approximately 500 m/s with a large uncertainty. The discrepancy is not unexpected, as the measurement is imprecise to hundreds of meters per second.

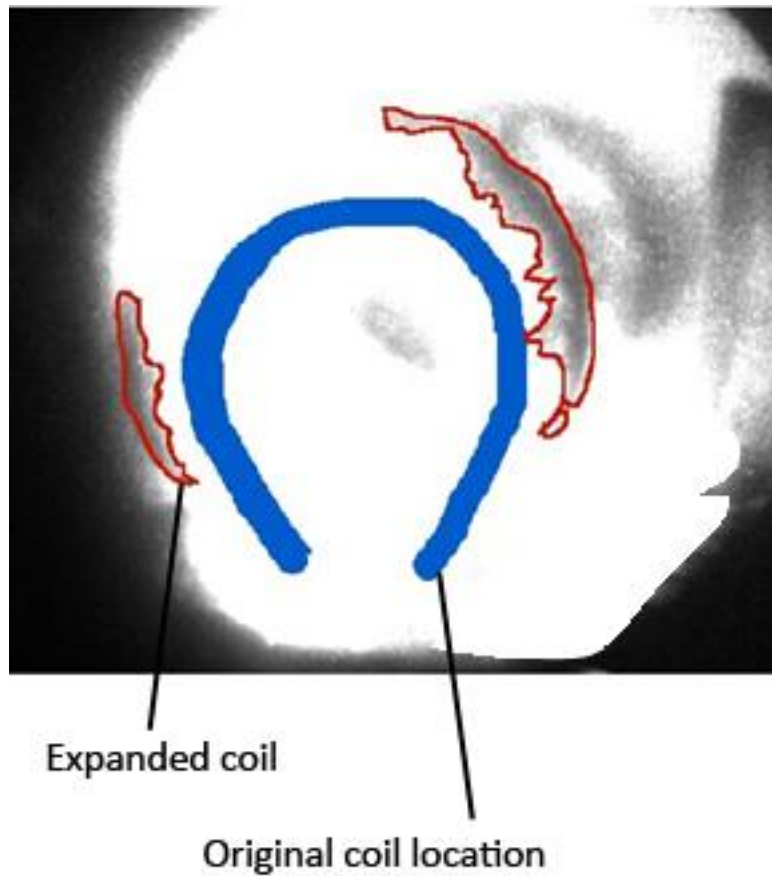


Figure 6.2 A fast framing camera image of a coil expanding. The coil fragments outlined in red are what is left of a thin coil 4 μ s after the trigger pulse. Distance traversed by the coil fragments is approximately 2 mm, indicating a velocity of \sim 500 m/s.

6.5 Qualitative Description of Coil Behavior

Coil behavior can be broken into three categories: Non-destructive mode, destructive mode with large fragmentation, and highly destructive mode. All of these behaviors are a function of coil cross section and current through the coil. Thinner coils and coils with smaller cross section become destructive at much lower currents. The majority of coils tested have a thickness of $1/8^{\text{th}}$ inch.

Coils operated at nondestructive currents deform after repeated use. In slotted coils the

two parallel loops will attract each other through dipole-dipole forces and pinch together. Calculations reveal that the timescale for this pinching is likely faster than expansion timescales. Figure 6.2 shows a slotted $\frac{1}{2}$ " ID coil after two nondestructive discharges of about 220kA.

Coils tend to pinch off and fragment into large pieces at slightly higher currents from about 500 to 700 kA. When a somewhat narrower segment of the coil is encountered, current is concentrated there. Heating weakens the metal and causes to deform, while the Z-pinch effect causes the surfaces of the coil to be attracted to each other. Combined with stretching of the coil as it expands, these effects cause segments of the coil to become thinner, concentrating the current further. This is a nonlinear effect that creates an instability similar to $M=0$ sausage instabilities in plasmas carrying current. It results in the coil splitting into fragments with sharp points.



Figure 6.3 This image shows fragments from a slotted coil that fragmented into pieces several millimeters in length. The ends of these fragments are often sharp from current concentration.

For solid coils at high currents, or perhaps with all multi-megaamp shots, there is very little left of the coil [23]. Conditions of this kind have not been tested on the system. Shots at 80 kV seem to produce destructive arcing in the transmission lines.

6.6 Skin effect

The skin effect is a high frequency current distribution effect for currents that are changing rapidly. It results from self-induced eddy currents that cause current to flow on the surface of metals. More generally, it is an effect of metallic dispersion of electromagnetic waves [35]. The skin effect in the Megagauss system causes current to flow primarily on the surface of the coil, and preferentially toward the inside surface. Initially it is concentrated on the inner outside edges, but as resistive heating progresses the metal conductivity lessens. Conductor temperatures reach several thousand Kelvin and copper is vaporized from these surfaces. This causes the current begins to flow more uniformly in the coil cross section. For very high currents well above 1 MA the coil vaporizes after several microseconds and no large fragments are found [35]. This regime has not been achieved on our system.

Skin depth can be approximated via the formula $\delta = \sqrt{2\rho/\mu\omega}$, where ρ is the conductivity, ω is the pulsed power frequency and μ is the magnetic permeability, which is close to μ_0 [35]. Most of the coils we have tested have been copper with a conductivity of $\rho = 1.68 * 10^{-8} \Omega\text{m}$. The angular frequency of the experiment can be approximated with the RLC ω or just using the current rise time of $1.7 \mu\text{s}$ as $1/4^{\text{th}}$ of the period. This formula gives a skin depth of about $420 \mu\text{m}$. Before significant Ohmic heating has changed the conductivity of the copper surface, this is the expected penetration depth of currents on the surface of the coils.

6.7 Comparison to Simulations and other Experiments

Rankin et al. at Loughborough University in the UK have carried out finite-element

analysis of single-turn coil behavior. They model the distribution of current and heating in these coils as a function of time and show how they affect coil expansion. Their results work well with low-current benchmark coils, whose deformation can be repeatedly measured [36]. They also agree well with the behavior of coils fired at lower currents in our experiments.

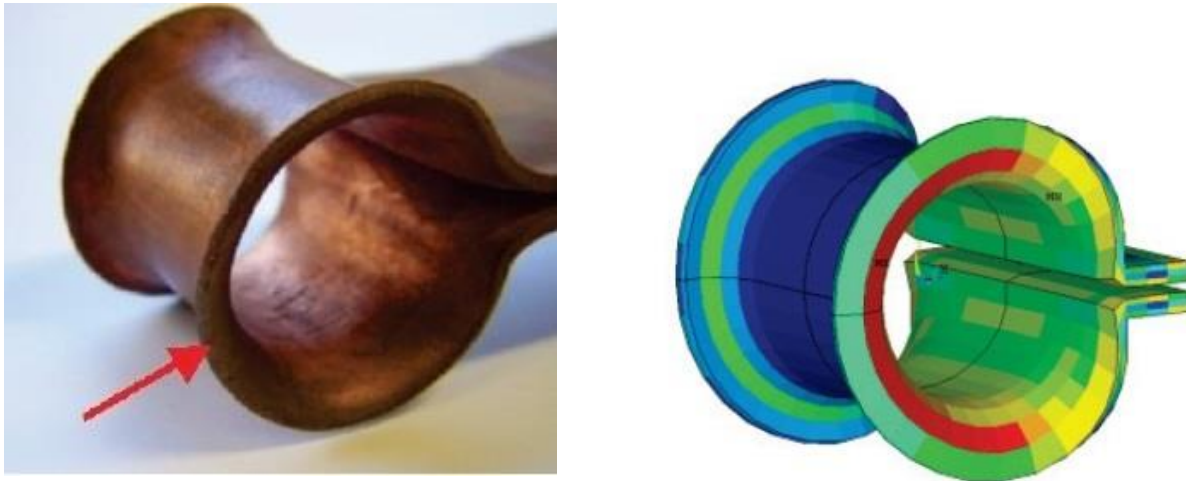


Figure 6.4 This figure shows a coil that has been subjected to a several hundred kiloamp discharge on the left. On the right is a simulation of the current distribution in the coil, with the peak current flowing on the outer inside surface [36]. Compare to Figure 6.5.



Figure 6.5 A bowed coil from a megagauss low-current shot on a 1/8th inch thick solid coil. This coil behavior agrees well with simulations and experiments done at other facilities as depicted in figure 6.5.

6.8 Expected Field from Known Currents

The magnetic field as a function of z in the early part of the current rise can be calculated from the current by modeling the coil as two separate wire loops with a fixed separation. Using the field from a single-wire loop, given by

$$B(z) = \frac{\mu_0 a^2 I}{2} \frac{1}{(z^2 + a^2)^{3/2}}$$

Where z is the position from the center of the coil on the z axis, a is the radius of the coil, I is the current through this loop, and μ_0 is the magnetic constant [22] [37]. This equation is in SI units. For reference, a thin wire loop with a radius of 1 cm carrying 1 MA of current will produce a field in the center of 132 T. We can superimpose two thin wire loops at a distance of $2l$ from each other and calculate the field along the z -axis as function of z . The result is the following equation [22] [37]:

$$B_z(z) = \mu_0 I a^2 \frac{1}{4} \left\{ [a^2 + (l - z)^2]^{-3/2} + [a^2 + (l + z)^2]^{-3/2} \right\}$$

Here I is the overall drive current, such that the current in each loop is actually $I/2$. For $l=a$, this field has a minimum at $z=0$ and represents a mirror-like configuration. This field z -axis profile would be an appropriate model if most of the current flows on the outer inside corners of the coils we use. A 1 MA total current would produce a 47 T field in the center and a peak field of 73 T near the middle of each loop, with a mirror ratio of about 1.5. These figures represent a design standard solid coil geometry, which uses a 0.93 cm (3/8th inch) inner diameter and a 0.93 cm long copper single-turn coil.

The magnetic field of a Helmholtz coil configuration comes from setting $a=2l$ in the

above equation:

$$B_z(z < a) \cong \frac{4}{5^{3/2}} \frac{\mu_0 I_d}{a} [1 + \dots + O(z/a)^4] \cong 0.358 \mu_0 \frac{I_d}{a}$$

Here I_d is the total current drive for the system similarly to before [22] [37]. The defining feature of the Helmholtz field is fairly uniform in the center regions. For comparison with the previous cases, the field in the center of a Helmholtz coil of inner diameter 1 cm at 1 MA is 94.7 T.

Finally, we can use the above methodology to integrate a continuous current distribution and produce a formula for the z-axis field for a finite solenoid of uniform current. The result is fairly complex:

$$B_z(z) = \frac{\mu_0 I}{4b} \left\{ \frac{b-z}{a_2 - a_1} \ln \left(\frac{a_2 + \sqrt{a_2^2 + (b-z)^2}}{a_1 + \sqrt{a_1^2 + (b-z)^2}} \right) + \frac{b+z}{a_2 - a_1} \ln \left(\frac{a_2 + \sqrt{a_2^2 + (b+z)^2}}{a_1 + \sqrt{a_1^2 + (b+z)^2}} \right) \right\}$$

Here, the length of the coil is $2b$ and the smaller and larger radii are a_1 and a_2 , while I is the total current through the volume [22] [37]. A uniform current description might be more appropriate after the surfaces of the coil have heated and deformed, causing more current to flow in the bulk of the copper conductor rather than on the surface [36]. For 1 MA uniformly distributed current in a 0.32 cm thick coil 0.93 cm long and 0.93 cm in diameter the peak on-center field is about 81

T.

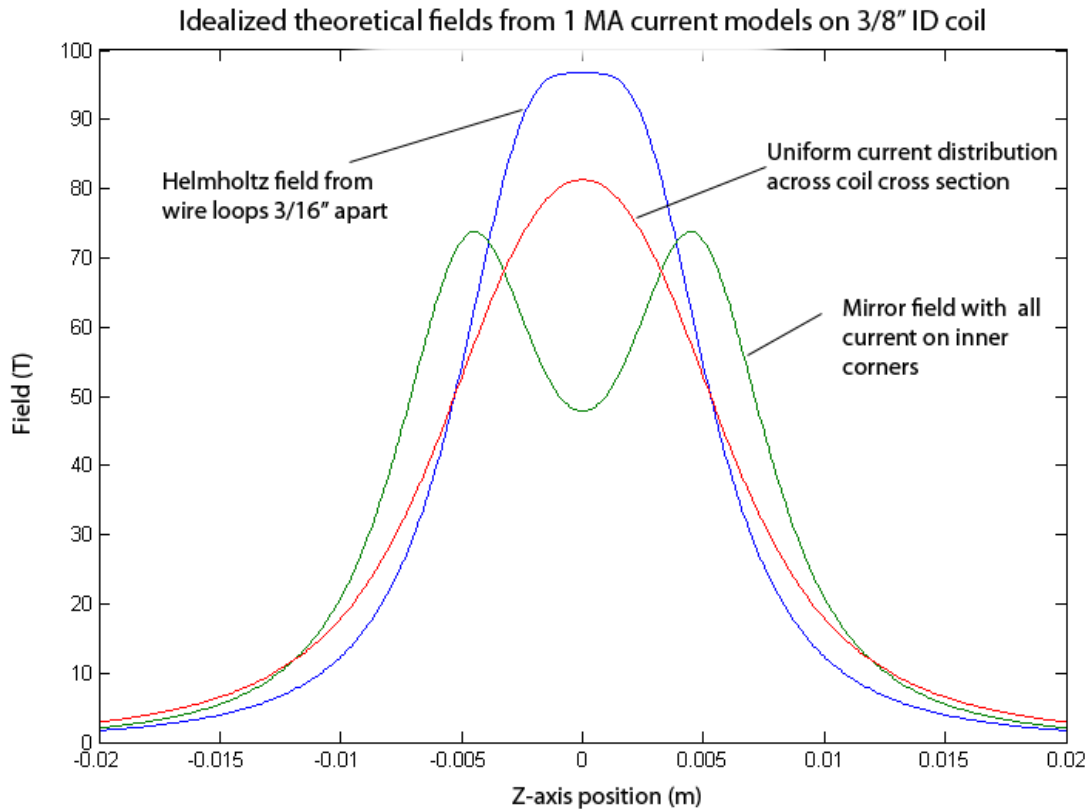


Figure 6.6 These four cases of field profiles for various current distributions using a total current of 1 MA. Blue is a Helmholtz configuration with a loop radius of 0.47 cm and separation of 0.47 cm. Green shows the mirror-like field for two loops separated by 0.93 cm, with a radius of 0.47 cm. This is a model in which the majority of the current flows on the outer inside edge of the coils. Finally, red depicts a uniform current distribution for coils of thickness of 1/8th inch.

Chapter 7: Faraday Rotation Measurements

7.1 Physics Background

There is a need for additional magnetic field diagnostics to ascertain both the magnitude of the magnetic field and its time behavior. The usual practice with megagauss fields is to use a Faraday rotation measurement. The application of a magnetic field in transparent solid materials produces the Faraday Effect, which is related to the Zeeman Effect. Using this as a diagnostic does not rely on inductive loops like B-dots, and makes a direct optical measurement of the field strength. A magnetic field creates a difference in the energy of electron sublevels. Left and right polarized light will excite different energy sublevels. This creates a polarization dependence in the dispersion relation. The net result is a change in the dielectric constant for left and right circularly polarized light. This causes index of refraction to be different for the left and right helicities propagating along the field lines, which is called birefringence. It causes left and right circularly polarized light to accumulate a phase difference as the two polarizations travel through the material. Linearly polarized light is a superposition of left and right circularly polarized light, so a rotation the polarization of a linearly polarized beam will appear. If the magnetic field is changing or increasing from zero, the total phase change increases with time and measures the field.

In practice, an initially linearly polarized laser beam can be sent through a Faraday rotation optic in a magnetic field and the polarization can be measured to get a value for the field. A strong field will make the polarization angle appear to rotate, often many times a full 2π radians. The polarization will be rotated by an angle that depends on the magnetic field strength,

the length of the magneto-optical material, and its material-specific Verdet constant v . That is, the rotation angle in radians goes like

$$\theta = v l B$$

where B is actually the value of the magnetic induction and l is the length of the crystal or Faraday medium. The Verdet constant is wavelength dependent. It has been measured accurately for many materials. It ranges from several radians per Tesla meter for common materials such as water and silicon dioxide in the visible range to over one hundred rad/T*m for terbium gallium garnet (TGG) or Terbium doped glass. TGG is frequently used in Faraday isolators, which are used to prevent back-streaming of beams in high power optics.

The rotation angle can be measured by placing a polarizing filter or polarizing element known as an ‘analyzer’ in front of a power meter device like a photodiode. The signal from the photodiode is proportional to the intensity of light. The intensity of light after the analyzer will follow a cosine squared function of the phase offset, of the form

$$I = I_0 \cos^2(\theta)$$

where I is the intensity, and θ is the polarization angle. This is called Malu’s law.

The Faraday rotation signal is useful for indicating the time behavior of the magnetic field. Since rotations will only occur while the field is changing, the polarization angle must be monitored continuously and the results recorded from the beginning of each measurement, when the field is zero. The field can be measured at every instant as the current from the pulsed power ramps up and decays away.

7.2 Experimental Setup

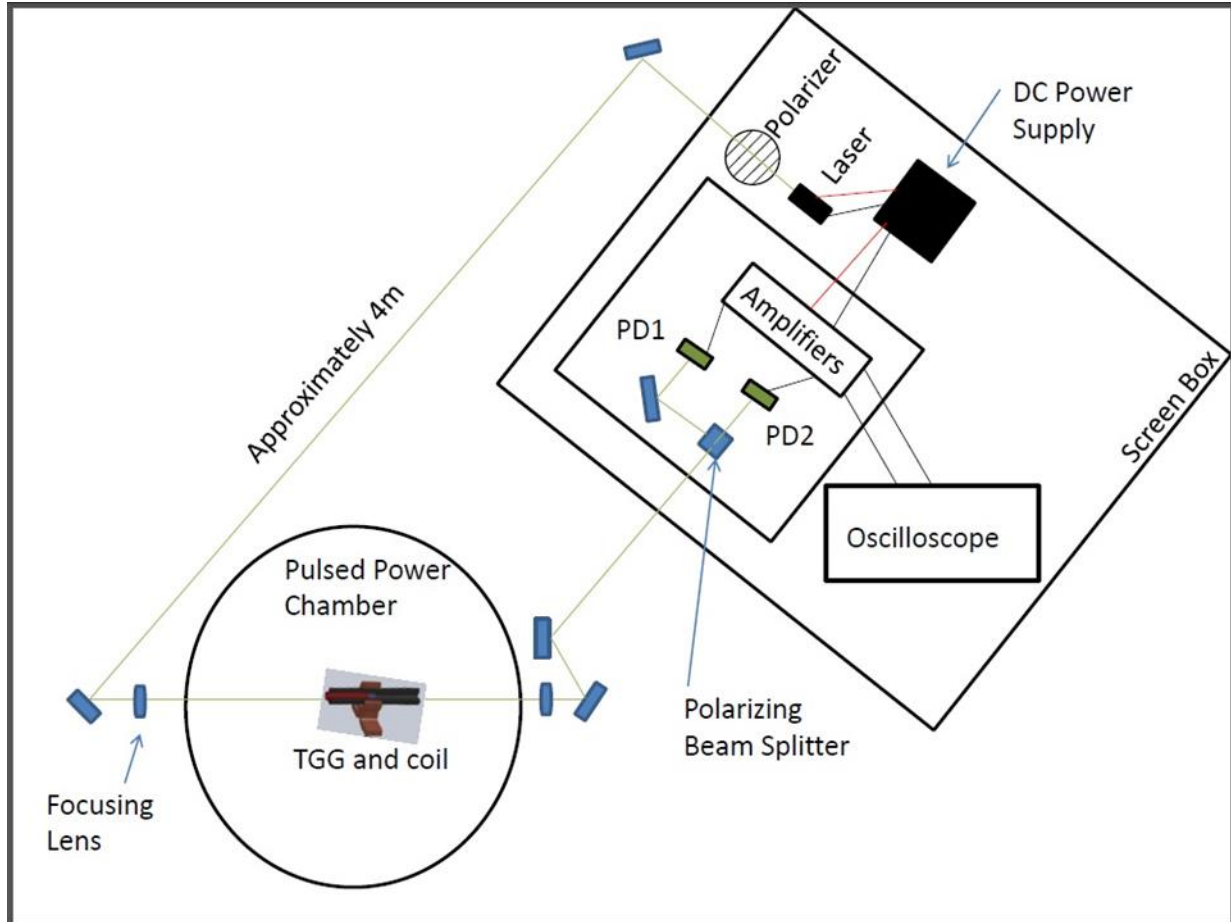


Figure 7.2 The final setup for Faraday rotation measurements, shown with correct relative orientation. All electronics related to producing and detecting the polarized beam are contained within a screen box. The laser beam is actually sent through periscopes and directed through holes in the screen mesh from above.

This magnetic field diagnostic requires a measurement of the change in the polarization angle of light from Faraday rotation. The basic hardware setup uses a polarized laser beam passing through the Faraday media in the variable field. The beam passes through an analyzing polarizer and a power meter, which reads the optical intensity electronically. The analyzer selects only a certain orientation of linearly polarized light for to be incident on the power meter.

While the Faraday Effect is a commonplace demonstration in many undergraduate physics labs, there are several differences that make this measurement more difficult. An

accurate count of the rotation angle as a function of time becomes the desired goal of the measurement, while the experimental challenges include mitigating electromagnetic interference (EMI). The most challenging aspect of gathering Faraday rotation data in this case is the electromagnetic interference (EMI) present. The worst of the noise is largely in the gigahertz range, and seems to be a result of the trigger pulse in the Maxwell trigger and spark gap switches. Lower frequency megahertz pickup is also present from the primary current pulse itself. For an unshielded BNC cable, the noise pickup is several hundred millivolts. The unshielded noise level is far beyond the 10 mV photodiode signal.

The experimental design must shield EMI while simultaneously amplifying the photodiode signal strength that reaches the oscilloscope. To this end, the optical setup allows the laser and detector to be far away from the pulsed power apparatus. Ultimately the EMI was reduced to sub- millivolt levels or less by placing the oscilloscope, photodiode, and laser inside a screen box. This screen box has filtered power and signal feedthroughs. A long cable outside the screen box picks up significant EMI from the Maxwell trigger generator. It acts as a trigger and is connected to the trigger signal used for the B-dot oscilloscopes.

A green 532nm 5mW CW diode laser pointer provides the beam. Though most lasers are initially linearly polarized, a polarizing filter improved the polarization by removing the off-linear components of the initial beam. This filter and the laser itself are rotated such that intensity is optimized and the light is polarized in the horizontal axis.

The Faraday medium is a 4 mm long TGG crystal (from Northrup-Grumman Synoptics overstock) that fits comfortably inside the smallest coils we planned to make. This crystal is short enough to avoid the potential problem of having too many rotations to be visible. A small crystal also has the added advantage of sampling the field in a smaller region. A 40 cm focal

length lens focuses the laser as it passes through the crystal.

To measure optical power, we used a pair of DET210 Thorlabs™ photodiode detectors. It is useful to be able to measure the two separate and orthogonal polarizations at once. To this end, the beam goes through a polarizing beam splitter to the two photodiodes and scope channels. The rotations on each channel are perfectly out of phase with each other.

The current through the photodiodes is proportional to optical power. Using such a 50 Ohm terminator and input impedance on the scope ensures that the RC time response of the circuit is fast enough to catch the megahertz oscillations of the Faraday signal. Unfortunately, given the fixed current behavior of the photodiodes this means that the photodiode signal voltage is quite low: a few millivolts or less. For this reason amplification electronics are necessary, followed by a buffer circuit. Keith Carter had fabricated a set of circuits using the Burr-Brown IC amplifier and buffer packages BB3553 and 3555. They are meant to be used together to accept a 50 ohm input impedance and drive a 50 ohm output impedance while still maintaining a reasonable gain and excellent frequency response. Each channel is configured for gain of 10 and a gain-bandwidth product of 1.7 GHz [38] [39]. The limitation of the system is actually the sampling rate of the TDS3054B oscilloscopes, which is 1000 points per microsecond [40].

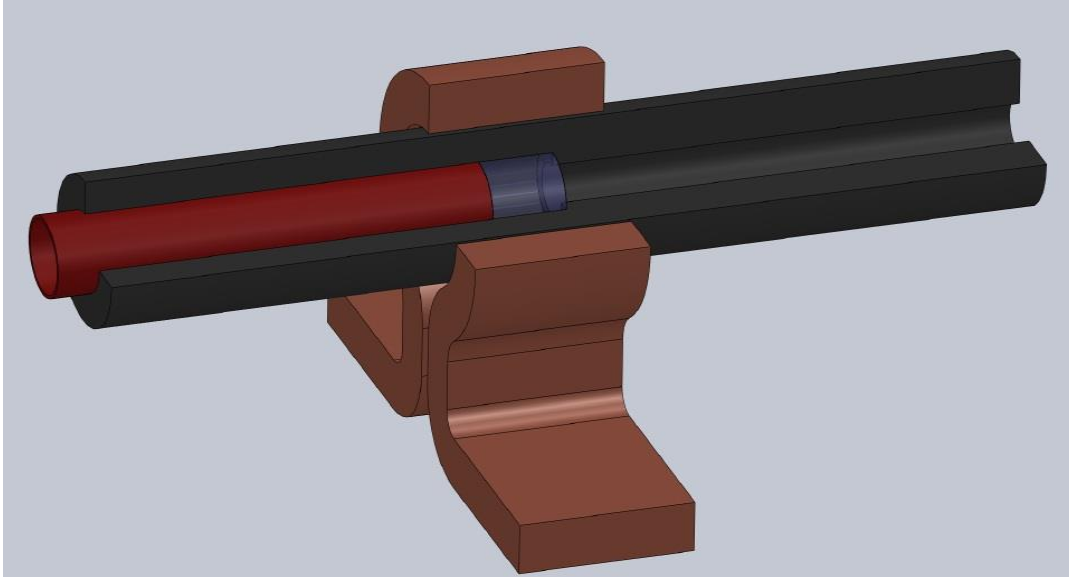


Figure 7.1 A SolidWorks™ cut-away view of a coil, Delrin rod, and Faraday medium. The crystal dimensions are 4 mm in length with a diameter of 4.8 mm. The coil length and ID is approximately 0.93 cm. The crystal is situated inside a Delrin™ tube which has been machined specifically to hold the crystal and protect it from copper dust and debris. An insert, shown in red, helps hold the crystal in place once. SolidWorks model by M. Wisher and S. Lewis.

7.3 MATLAB Analysis

We Analyze the Faraday rotation data to translate the optical intensity time series data into a magnetic field as a function of time. It is mainly a matter of counting accumulated phase by counting oscillatory ‘fringes’ in intensity from the beginning of the signal. As time proceeds, the field increases, and the angle of polarization accumulates. The rotations in polarization are counted by adding a factor of π rather than 2π for every period because intensity goes like cosine squared of the rotation angle, as described in section 7.1. Stated another way, every Faraday ‘rotation’ is a phase change of 2π and produces two complete oscillation periods in measured intensity. Once the peak field is reached, the accumulated phase “unwraps” or rotates in the opposite direction. The magnetic field measured is directly proportional to the accumulated phase. Section 7.1 explains this in more detail.

Step by step, I will describe the algorithm used to extract the accumulated phase from the raw data. The raw data is initially obtained from the oscilloscope using LabView™ software. This generates a comma separated value file that can be read into Microsoft Excel™ and saved in .xlsx format. The MATLAB script reads the data from excel and does the majority of the analysis on the rotation data. First, to remove some noise, the data is smoothed with a running mean of neighboring points. To ensure that the oscillatory data is readable, the program automatically subtracts away the mean of the overall data. The result is an oscillatory signal with relatively consistent amplitude, centered about zero.

The rotations or fringes can then be counted to measure the field. The algorithm searches for zero-voltage level crossings. It does this by searching for neighboring points of opposite sign. Counting zero crossings by itself would be sufficient to count rotations in half-pi phase additions. Or, the same result can be achieved by counting maxima and minima. This code does both. It finds extrema by looking for the highest value in each region between zero-crossings. If the data between a zero-crossing is greater than zero, it searched for a maximum point. If more than one point is a maximum, it selects the first of the set of maximal points. It does the analog for minima. The values of these extrema in each region are used to normalize the data. Peaks are counted, starting from zero, to measure the total number of rotations. The field increases up to a specified turn around point defined by the user in the code, at which point the accumulated phase from each rotation gains a negative sign to decrease the field with each rotation.

It is useful to be able to plot a well-defined B-field data point for each moment in time. The field value from rotation between integral steps of pi can be filled in. The algorithm takes the normalized data directly and performs the arc cosine between each peak. To avoid making arc cosine multi-valued, it is normally only defined in the region from -1 to 1 in the range from –

$\pi/2$ to $\pi/2$. The range can have an incorrect sign depending on whether phase is accumulating or diminishing, and whether a maxima precedes a minima. The code takes this into account. The result is a representation of phase between each interval step that uses each data point directly. A plot of $B(t)$ can be generated with the correct units and scaling by dividing by the Verdet constant and length of the crystal. For TGG I used a value of 184 rad/Tesla*m at a wavelength of 532 nm. The plots match very closely with plots of current as a function of time as obtained from B-dot data.

7.4 Results in Atmosphere

A handful of Faraday rotation shots so far have allowed us to verify both the expected time behavior and overall amplitude of the field in the coils. All of our successful Faraday rotation measurements have occurred with the chamber in atmosphere. Vacuum operation has yet to be successfully demonstrated. It is important to note that any fields measured by Faraday rotation are actually line-integrated averages over the length of the crystal. We have measured a peak field in the center of the coil of approximately 65 T for solid coils of 3/8th inch diameter. This field value is based both on MATLAB analysis and evaluation by counting rotation peaks.

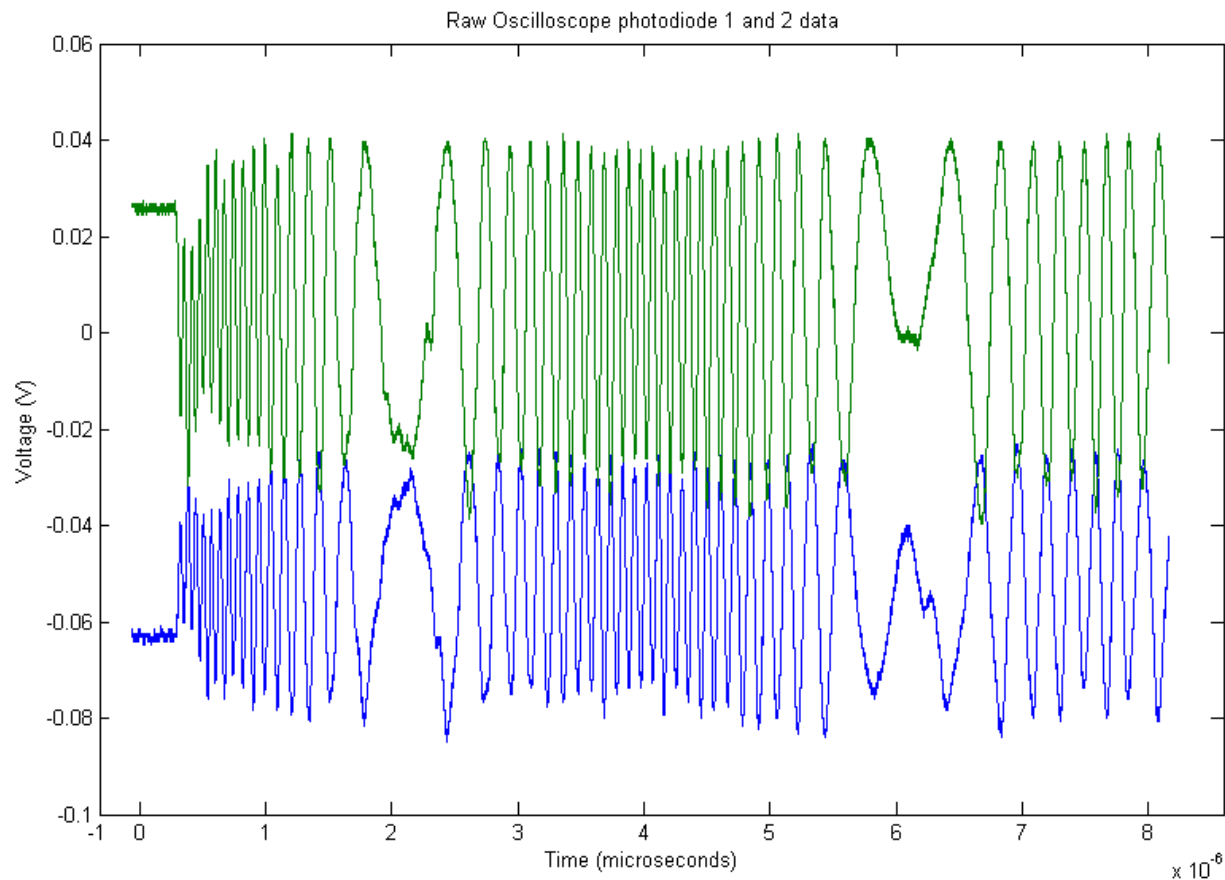


Figure 7.3 Raw oscilloscope data from shot 421, with the crystal approximately on center, showed 15.5 rotations. To calculate the peak field from this, we do $(15.5\pi \text{ rad}) / ((190 \text{ rad/T}\cdot\text{m}) \cdot (0.004 \text{ m}))$ to yield an average field about 64 T in the 4 mm region around the center of the coil. This was for a shot with a peak current of 1.03 MA and a rise time of 1.88 μs .

In these shots, the initially solid coil would typically fragment into a few fairly large pieces. In a few cases, switch failures led to currents of only about 800 kA, and in some of those cases the coils would separate and expand but not break entirely. Neither the magnetic field nor the B-dots show any obvious effects on microsecond time scales from coil expansion, which is to be expected. The coils seem to break after the field measurements are complete. Understanding of the peak fields and z-axis profiles using current models leads us to the conclusion that a portion of the coils vaporizes on sub-microsecond timescales, as described further in section 7.5.

MATLAB analysis produces an approximate picture of the current as a function of time. This allows a comparison with both switch current b-dot sum signal and load b-dot signal. The integrated b-dot signal, which should follow the magnetic field and current, corresponds closely in time and functional shape. Both functions can be fitted to a decaying sinusoidal function. The Faraday rotation signal can in principle be used to deduce the inductance and other circuit parameters.

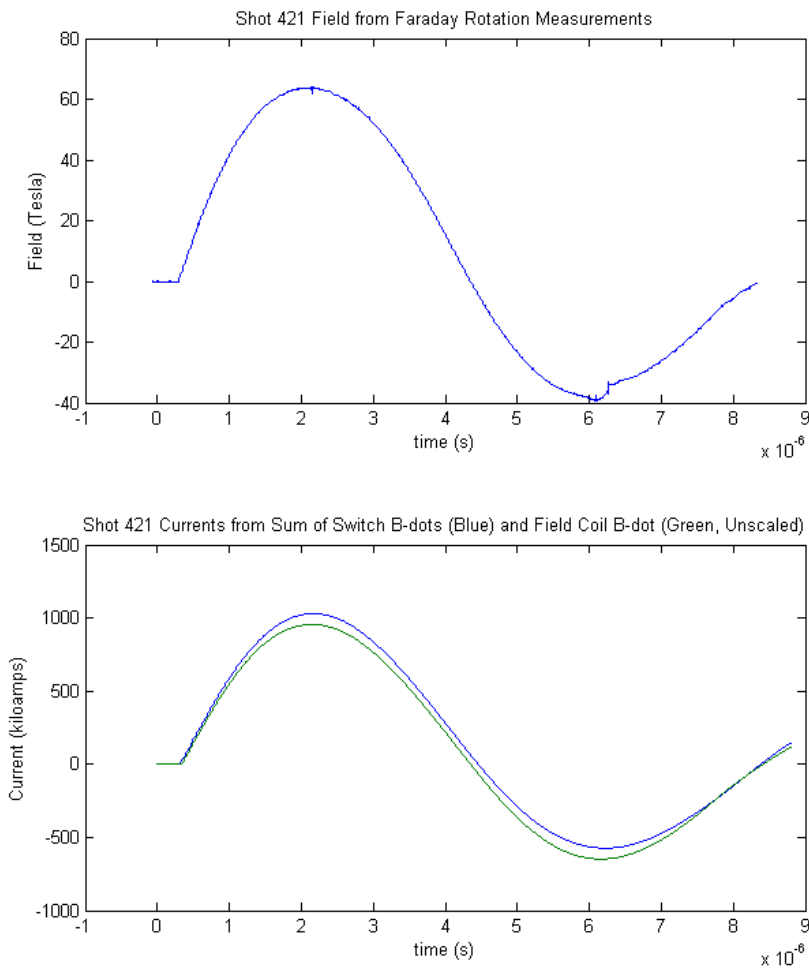


Figure 7.4 The magnetic field as a function of time, as measured by Faraday rotation and interpreted using MATLAB. Below is a plot of the current as a function of time. The plots below measure the induced voltage from B-dot probes.

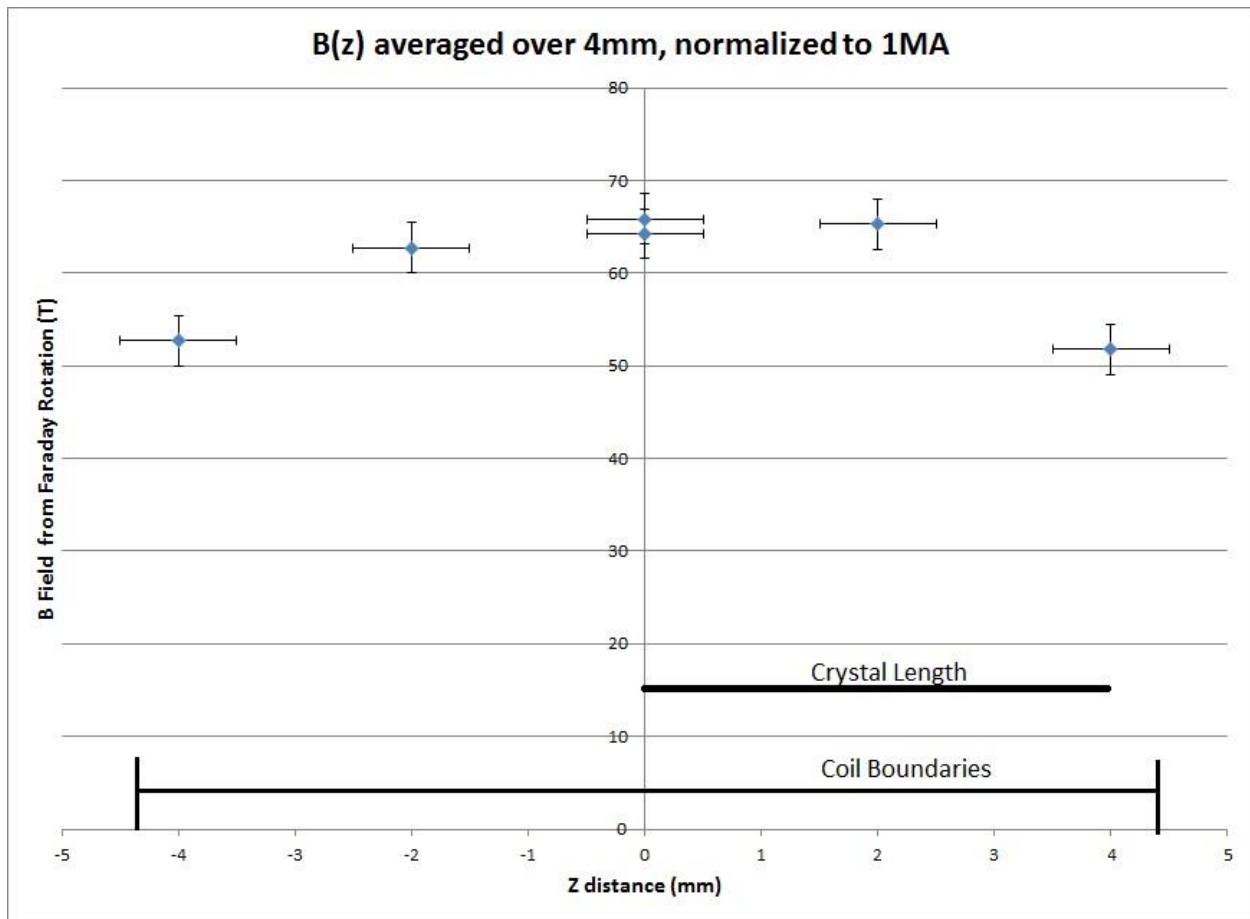


Figure 7.5 Peak magnetic fields as a function of the z-axis location of the TGG crystal. The coil dimensions are 0.93 cm ID and 0.93 cm length. The rotation optic was translated in 2 mm increments in each direction from center, providing a measurement of the field averaged over the length of the 4 mm crystal in each direction. Uncertainty in B comes mostly from a 3% uncertainty in knowledge of the Verdet constant at 532 nm. From left to right, the represented shots are 417, 426, 416, 421, 427, and 418.

7.5 Field as a function of position on the Z-axis

There are several experimental questions we can explore using Faraday rotation data. Our measure of the peak field allows some degree of spatial resolution of the single-turn coil field. We can translate the Faraday crystal horizontally in the z-axis to explore the field profile. Such measurements are unique because most groups have used a long Faraday rotation fiber that

passes through the entire coil as an absolute measurement of field intensity. This gives an averaged field over the entire coil and will not inform us strongly of the current's spatial behavior in the coil. The TGG crystal samples an averaged field over the relatively short 4 mm length of the crystal. The length is short enough that we can create a field profile as a function of the crystal's position on the z-axis and compare this measurement to expected fields from various current distributions.

In order to compare a predicted field to the Faraday rotation measurements, averaging must be performed on the expected fields. We can do this with numerical integration over the crystal length:

$$\int_{z_0-2\text{ mm}}^{z_0+2\text{ mm}} B(z)dz$$

When this 4 mm smoothing is taken into account, several different 1 MA models for the current distribution are shown in figure 7.6 compared to the peak field rotation data in figure 7.5. We can rule out a model with current flowing exclusively on the outer inside edge of the coils. Such a current distribution would produce a characteristic dip in field strength towards the center that is not observed. When the original coil dimensions are used, the fields are approximately 20% larger than the measured peak fields. This discrepancy can be accounted for by supposing that the current has moved out to a larger radius, as would occur if the inner surface of the coil has boiled off from Joule heating. The lower-amplitude curve in each color in figure 7.6 describes a field produced by new dimensions, in which the current radius has been moved outward by 1.5 mm. The field shapes are largely preserved. For these simplistic models, the profile that matches most closely comes from a uniform current distribution with a modified inner coil radius.

The literature describes models of current distributions with finite solenoid loops with their own inductance. These models show current flowing primarily on the inner surface and outer faces, which also evolve in time [36]. I created two simplified models of current flow in the coil using a square mesh of the coil cross section and a current distribution that followed a fourth order polynomial of position in z (for the first model) and both r and z for the second model. For the second model, the current peaks along the inner surface and falls off like a negative fourth order polynomial, reaching zero at the outer radius. The full 2D current distribution in the cross section is qualitatively meant to follow the current distribution work of Novac et. al. [36]. Figure 7.7 shows our simulated current as a function of z . Our simulated current consists of 400 filaments according to the function show in the figure with the sum current normalized to 1 MA. We can compute the field as a function of z for an arbitrary current in MATLAB by computing the z -dependent fields of narrow filaments using

$$B(z) = \frac{\mu_0 a^2 I_{i,j}}{2} \frac{1}{(z^2 + a^2)^{\frac{3}{2}}}$$

and summing over all filaments. The procedure is equivalent to integrating these fields and performing linear superposition. We then use a 4 mm smoothing of the field profiles to compare these modeled fields with Faraday rotation data. Figure 7.8 is the result of these attempts at more realistic field profiles. These profiles have used an inner radius for the current of 1.5 mm from the original inside surface of the coil. This simulates the removal of material from the inner surface and corners through Joule heating, and removes a significant 15-20% discrepancy in the modeled peak field and the measured peak field. Rotation data fits most closely with a current distribution model in which the 1 MA of current has r dependence and has moved outward by more than 1 mm. Overall agreement between models as based on the literature and the field

profile measurements is relatively good. We believe we have a good understanding of the behavior of the fields in these single turn coils and an accurate way to measure them.

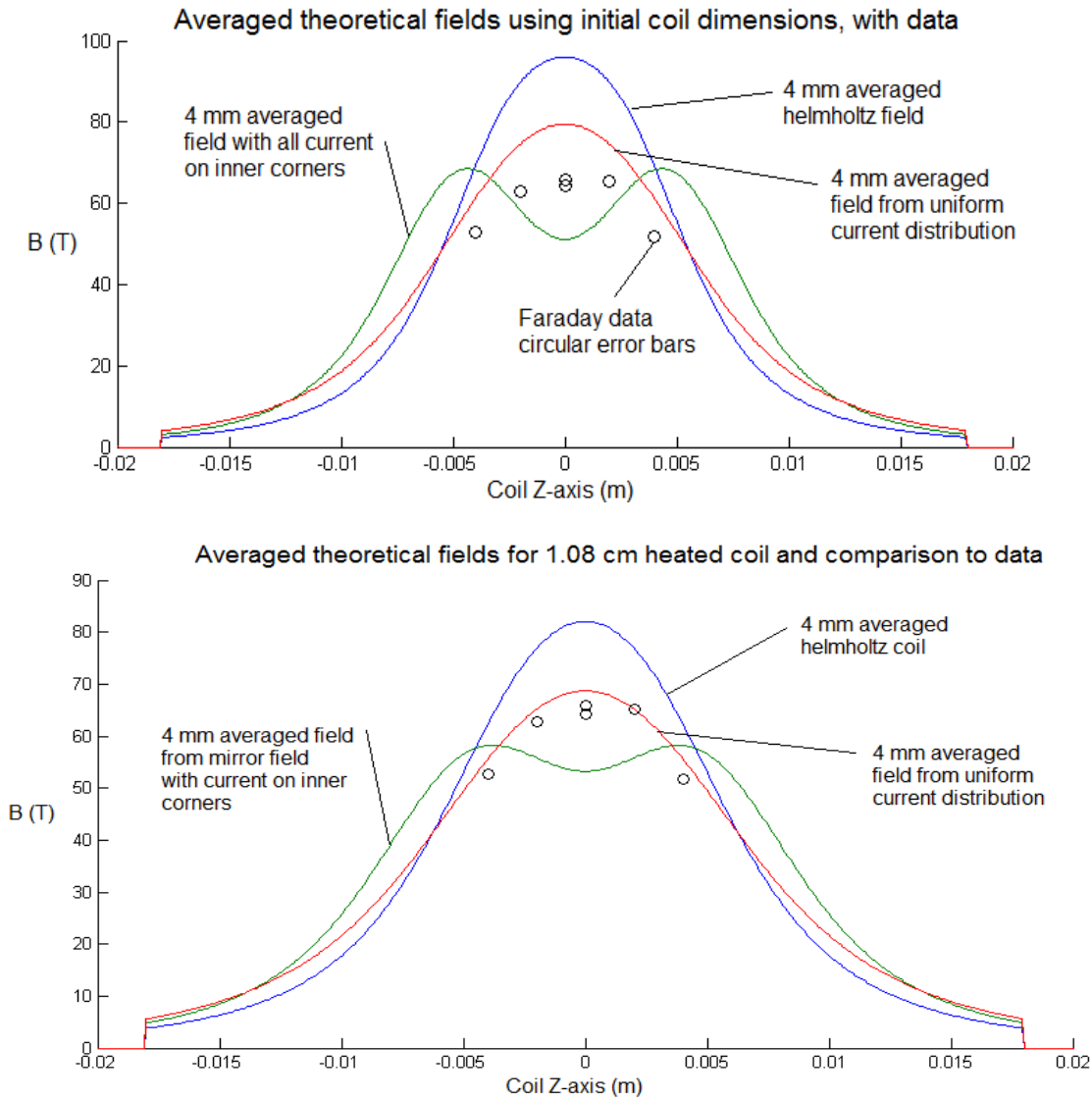


Figure 7.6 This figure is a running average over the crystal length, performed with numerical integration, of the plots depicted in figure 6.7. The average is over a 4 mm interval to simulate what the TGG crystal would measure when it is placed with its center at each location on the Z-axis. The models are compared with sets of peak-field data, again normalized to 1 MA. The inner radius of the coil has been adjusted between the two plots. The first plot uses the original coil dimensions with a 0.93 cm diameter. A coil with an inner surface removed to a depth of 1.5 mm is a better fit to Faraday rotation data.

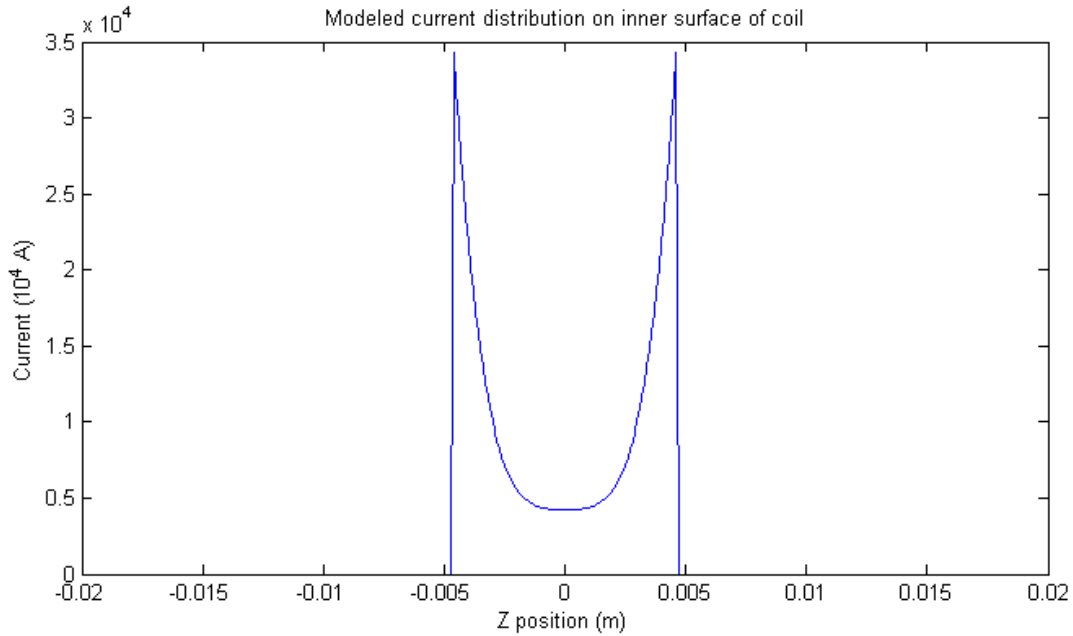


Figure 7.7 This model of the z-axis current distribution on the inner surface of the coil produces the most field profile match to the B(z) data. This current distribution is a fourth-order polynomial in z, and is normalized to 1 MA. Polynomial coefficients were adjusted iteratively to give an averaged current profile that was similar in shape to data.

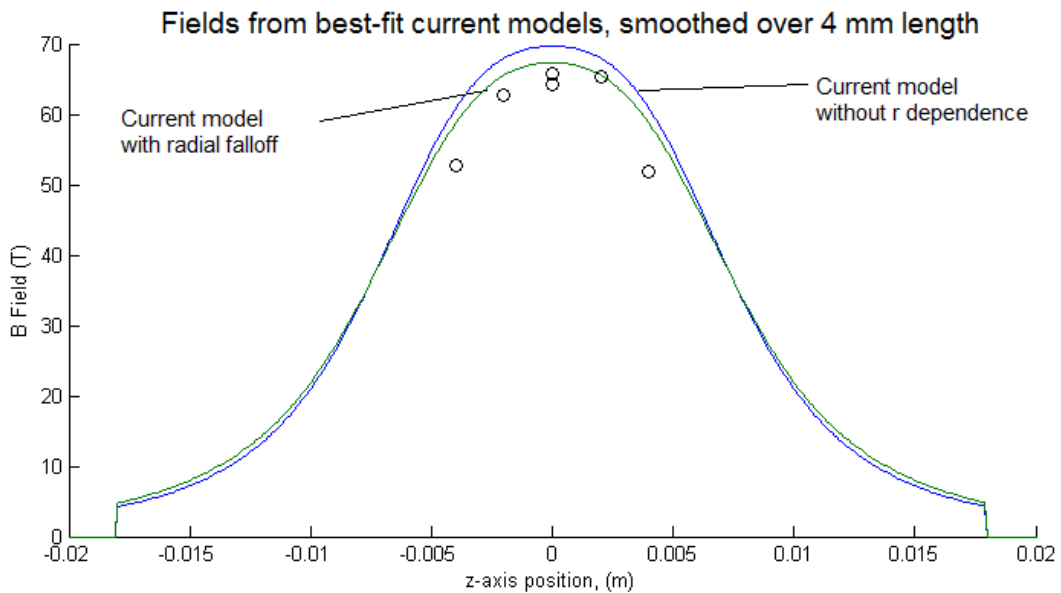


Figure 7.8 These field profiles use the z-dependent current profile from figure 7.7. These field models use an inner radius that has increased by 1.5 mm from the initial coil inner radius, to a value of 1.08 cm. They are smoothed over a 4 mm length to match measurements. The lower, green curve represents a current distribution that falls off in r, while the blue profile is entirely along a 2D cylinder at 1.08 cm radius. The field profiles are again compared to Faraday rotation data.

Chapter 8: Conclusions

Collaboration between the University of Texas and Sandia National Laboratories has produced a pulsed power device for laser plasma experiments. This system is intended to produce strong magnetic fields for confining laser-generated plasmas. These cluster fusion plasmas are at fusion temperatures of ~ 10 keV and densities of nearly atmospheric density. Such a uniquely hot, dense plasma produces a tremendous thermal pressure, so only magnetic fields on the order 100 Tesla will confine them. This requires pulsed power to deliver intense current to a field coil before it blows itself apart from magnetic pressure. The pulsed power apparatus must also deliver this field in vacuum.

We have helped Sandia construct such a device and we tested it at UT. It is theoretically capable of delivering more than 2 MA of current to a load such as a magnetic field coil. The design is a basic RLC circuit with a capacitance of 31 μF and an inductance of about 50 nH. Sandia National Laboratories made this equipment possible with their expertise in design and construction of pulsed power.

Testing has revealed that we can deliver more than 1 MA of current to a load in atmosphere, and with somewhat unreliable performance in vacuum after modifications made by M. Wisher. We have observed coil destruction behavior and found that it is consistent with the fields we expect. Trouble with breakdown has hindered accessing the full theoretical capabilities of the apparatus.

Faraday rotation measurements indicated that the peak field at a charge voltage of 50 kV is approximately 65 Tesla. We have characterized the field as a function of time and found that it roughly follows the expected RLC damped sinusoidal function proportional to the current. Time-resolving Faraday rotation measurements allow us to diagnose the effects that breakdowns might

have on the fields in the coil. We have mapped fields as a function of z-axis position and found them consistent with expectations, noting that some resistive heating may be occurring in the coils.

Development work continues and a laser experiment run on the Texas Petawatt is scheduled for May of 2013.

Appendix A: Megagauss System Pre-Shot Checklist

Items in *italics> are necessary for vacuum shots.*

1) *Bring chamber to operating pressures.*

Pressures less than 1 mTorr. Above these pressures the transmission lines are heavily susceptible to breakdown. This involves roughing the chamber, closing the roughing line, and engaging a turbo pump.

2) Prepare system electronics.

- a) Turn on the three B-dot monitor scopes in the scope rack. There is a B-dot for each switch and one additional B-dot for the load, so 11 channels are necessary for a full system shot.
- b. prepare and turn on any additional electronics required

3) Start LabVIEW™ Megagauss Control software.

It is also necessary that the compactRIO be on and network communication with multiple scopes be set up.

4) Deliver pneumatic supply pressure to the Fast valve (for vacuum shots with debris)

The fast valve requires a supply pressure of between 50 and 70 psi.

5) Prepare the pulse valve for cluster delivery (for gas jet shots)

This includes setting up an appropriate delay on a SRS delay box, which ordinarily is set up to first trigger the fast valve about 16 ms before then triggering the pulse valve and the Maxwell trigger. The Iota One pulse valve driver must be configured in single-shot external trigger mode. The pulse valve must have appropriate backing pressure supplied to it.

6) Pressurize the switch can assemblies.

Conventional operation uses a mix of SF₆ gas and dry N₂. Ordinarily we do not purge atmospheric gasses from the switch cans to begin with, but this can be done by flushing N₂ through the vent lines. The required pressure of SF₆ in the cans can be as low as 1 psig, but typical values are between 1 and 2 psig. The cans are then topped off with 3-4 psig of N₂ for a total of about 5 psig.

7) Open the dry air supply.

Use only Ultra-Zero grade dry air for pressurizing the switches and providing air to the Maxwell Trigger Generator. Ensure that the Maxwell Trigger has a nonzero dry air flow by looking at the flow meter on the front panel.

8) Pressurize the switches using the LabVIEW control VI.

The switches must have a set pressure of dry air for discharging properly at each voltage. The pressure range is fairly narrow, approximately 5 psig. Too high a pressure and the switches will not trigger at all. Too low a pressure and they are likely to pre-fire. Typical operating pressure at 50 kV is 42psig. Operating pressure should scale roughly linearly with voltage, however for lower voltages the system is comparatively harder to trigger so proportionally lower pressures must be used. 18-20 psi is a good operating range for 30 kV.

9) Turn on the Maxwell Trigger Generator

The Maxwell has a built in timer that does not allow its high voltage circuitry to be turned on until several minutes after the device itself is turned on. It also has a keyed interlock as an additional safety precaution. When this keyed interlock is engaged vertically, and the filaments are ready button is engaged, high voltage can be turned on.

10) Retract the shorting levers.

These levers are spring-loaded and normally ground the capacitor terminals. They are retracted with red handled pins that have long red warning ribbons on them. Once these pins are engaged in all 10 capacitors, the system may become charged. If even one of the shorting levers is still retracted, it will provide a path to ground through the relay tank resistor network and none of the capacitors can become charged unless a connection has been broken.

11) *Ensure that the gate valve in front of the turbo pump is closed before taking the shot. This protects the turbo pump from high velocity debris and dust that could destroy the pump. Normally chamber pressure rises in the minute that the turbo pump is closed, and steps must be taken to ensure that the pressure does not rise too much in this time.*

12) Arm the system.

These are the final steps to prepare for a shot.

- a) Turn on the power on the Glassman HV Supply.
- b) Enable the Maxwell keyed interlock, and flip the HV toggle switch to “On”.

13) ALL personal must EVACUATE the room once the system is armed.

14) Set the charging parameters

- a) Set the charge current to 30 mA.

This is the maximum current that can be supplied by the Glassman. Charge time for a full-system 10 –capacitor shot is approximately a minute.

- b) Set the charge voltage.

15) Open the Dump Relay via the control software.

16) Enable the high voltage.

The capacitor charge voltage and charge current will show up in the VI with green bars. Once the charge voltage reaches close to the set value, and the charge current settles to nearly zero, the system is charged and ready to fire.

17) Fire the system by pressing the Maxwell Trigger button.

Appendix B: Megagauss System Post-Shot Checklist

- 1) Ensure that the Dump Relay is closed.
The button on the LabVIEW™ control VI will show green. This is the first safety step that allows personal to re-enter the room with the system.
- 2) personel re-entering the room must **turn off Glassman HV supply and all Maxwell Trigger toggle switch options.**
- 3) Remove the pins that hold the shorting levers open.
This ensures that all the capacitors now are grounded.
- 4) Turn off dry air supply to prevent unnecessary waste.
- 5) Ensure that all oscilloscope data gets saved.
LabVIEW™ VI s have been written to download scope data rapidly.
- 6) *Vent the chamber* and proceed to examine the shot
- 7) Clean transmission lines and replace coil for new shot.
Refurbishment is the most time-consuming aspect of performing multiple shots.

Bibliography

- [1] T. Ditmire and e. al., "*High-energy ions produced in explosions of superheated atomic clusters*", 1997.
- [2] T. Ditmire, J. Zweiback, V. P. Yanovsky, T. E. Cowan, G. Hays and K. B. Wharton, "'Nuclear fusion from explosions of femtosecond laser-heated deuterium clusters'", *Nature* 398, 489-492, 1999.
- [3] J. Zweiback and e. al., "'Detailed study of nuclear fusion from femtosecond laser-driven explosions of deuterium clusters'", *Phys. Plasmas* 9, 3108-3120, 2002.
- [4] T. Ditmire and e. al., "'High-Energy Ions produced in explosions of superheated laser-driven explosions of deuterium clusters'", *Phys. Plasmas* 9, pp. 3108-312, 2002.
- [5] J. Zweiback, T. E. Cowan, R. A. Smith, J. H. Hartley, R. Howell and C. A. Steinke, "'Characterization of fusion burn time in exploding deuterium clusters plasmas'", *Phys. Rev. Lett. Vol 85, Num 17*, 2000.
- [6] *Personal communication with Prof. Roger Bengtson, University of Texas at Austin.*
- [7] e. a. I. Loupasakis, "*MHD computations for plasma trapping in open magnetic field devices for high neutron flux production*", *35th EPS conference on Plasma Phys. Hersonissos, 9-13 June 2008 ECA Vol.32D, P04.116 (2008)*, 2008.
- [8] S. Moustazis and P. Lalouis, "*On the expansion of high density plasmas in mirror-like magnetic topologies*", 2009.
- [9] L. Perkins, B. Logan, M. Rosen, M. Perry and T. D. d. I. Rubia, "The investigation of high intensity laser driven micro neutron sources for fusion materials research at high fluence," *Nucl. Fusion* 40, 1, 2000.
- [10] K. W. Madison, P. K. Patel, M. Allen, D. Price and T. Ditmire, "Investigation of fusion yield from exploding deuterium-cluster plasmas produced by 100-TW laser pulses," *JOSA B, Vol. 20, Issue 1, pp. 113-117.*, 2003.
- [11] *Personal Communication with Dr. Woosuk Bang, UT Austin.*
- [12] B. N. Breizman and A. V. Arefiev, "Electron Response in Laser-Irradiated Microclusters," *Plasma Physics Reports*, vol. 29, no. 7, pp. 593-597, 2003.
- [13] B. Breizman and A. Arefiev, "Ion acceleration by hot electrons in microclusters," *Phys. Plasmas* 14, 073105, 2007.
- [14] K. e. a. Madison, "Role of laser-pulse duration in the neutron yield of deuterium cluster targets," *Phys. Rev. A, 70:053201*, 2004.
- [15] E. Gual and e. al., "Demonstration of a 1.1 petawatt laser based on a hybrid optical parametric chirped pulse amplification/mixed Nd:glass amplifier," *Applied Optics Vol. 49, Iss. 9, pp. 1676-1681*, 2010.
- [16] W. Bang, *Cluster Fusion Experiments on the Texas Petawatt Laser*, Austin, Texas, 2012.

- [17] O. F. Hagena and W. Obert, "Cluster Formation in Expanding Supersonic Jets: Effect of Pressure, Temperature, Nozzle Size, and Test Gas," *J. Chem. Phys.* 56, 1793, 1972.
- [18] O. F. Hagena, "Cluster ion sources," *Rev. Sci. Instrum.* 63, 2374 (1992), 1992.
- [19] *Personal Communication with Prof. John Keto, UT Austin.*
- [20] *Personal communication with Prof. Boris Briezmann, University of Texas at Austin.*
- [21] *Personal communication with Dr. Hernan Quevedo, UT Austin.*
- [22] K. Struve and e. al., *Megagauss Field Generation for High-Energy-Density Plasma Science Experiments*, 2008.
- [23] F. Herlack and N. Miura, *High Magnetic Fields: Science and Technology Vol. I Methods and Techniques*, Singapore: World Scientific Pub. Co. Pte. Ltd, 2003.
- [24] O. Portugall, N. Puhlmann, H. U. Muller, M. Barczewski, I. Stolpe and M. v. Ortenberg, "'Megagauss magnetic field generation in single-turn coils: new frontiers for scientific experiments,'" *J Phys. D: Appl. Phys.* 32 (1999) 2354-2366," *J Phys. D: Appl. Phys.* 32, pp. 2354-2366, 1999.
- [25] O. Portugall, N. Puhlmann, H. U. Müller, M. Barczewski, I. Stolpe, M. Thiede, H. Scholz, M. v. Ortenberg and F. Herlach, "'The design and performance of a transportable low-cost instrument for the generation and application of megagauss fields.'" *J. Phys. D: Appl. Phys.* 30 (1997) 1697-1702," *J. Phys. D: Appl. Phys.* 30, pp. 1697-1702, 1997.
- [26] J. Wosnitza and e. al., "'Dresden pulsed magnetic field facility,'" *Journal of Magnetism and Magnetic Materials*, Vol 210:2 2728–2730, 2007.
- [27] K. Struve and e. al, *LDRD Final Report on Confinement of Cluster Fusion Plasmas with Magnetic Fields*, 2011.
- [28] O. Gotchev and e. al., "Magneto-inertial approach to direct drive laser fusion," *J. Fusion Energy*, vol. 27, pp. 21-31, 2008.
- [29] e. a. R. B. Spielman, "PBFA II-Z: A 20-MA Driver for Z-pinch Experiments," in *in Proc. of the 12th IEEE Int. Pulsed Power Conf.*, 1995.
- [30] M. L. Wisher, *Megagauss: A Portable 40T Magnetic Field Generator*, Austin: University of Texas at Austin, 2011.
- [31] *Personal communication with Brian Stoltzfus at Sandia National Laboratories.*
- [32] *Personal communication with Matthew Wisher.*
- [33] *Personal commincation with Dr. Kenneth Struve, Sandia National Laboratories.*
- [34] *National Instruments*, 11500 N Mopac Expwy Austin, TX 78759.
- [35] J. D. Jackson, *Classical Electrodynamics*, 3rd edition, John Wiley and Sons, 1998.
- [36] D. F. Rankin, B. M. Novac and I. R. Smith, "Three-dimensional finite element alanysis of single-turn coil systems," in *IEE proceedings- Science, Measurement and technology*, Vol 153, 3, Loughborough, 2006.

- [37] H. E. Knoepfel, *Magnetic Fields*, New York: John Wiley and Sons, 2000.
- [38] Burr-Brown, *BB3554 Datasheet*, 1983 Burr-Brown Corporation, 1993.
- [39] Burr-Brown, *LH0063/BB3553 Datasheet*, 1993.
- [40] Tektronix, *TDS3000B Series Digital Phosphor Oscilloscopes User Manual*, Beaverton OR, 2003.

Vita

Sean Matthew Lewis was born in Bloomington, Indiana, in the United States in 1987. He attended Bloomington High School North, graduating in 2005. From 2005 to 2009 he attended Indiana University in Bloomington, receiving bachelor's degrees in physics and mathematics. From 2009 to present, Sean has attended the University of Texas at Austin for graduate work in Physics.

Permanent Address: Sean Lewis
4802 Clarkson Ave
Austin, TX
78751
sealewis@gmail.com

This Thesis was composed in Microsoft Word™ by the author.